G10/COSMOS: 38 band (far-UV to far-IR) panchromatic photometry using LAMBDAR

S. K. Andrews,[1][⋆] S. P. Driver,[1,2] L. J. M. Davies,[1] Prajwal R. Kafle,[1] Aaron S. G. Robotham[1] and Angus H. Wright[1]

[1]*International Centre for Radio Astronomy Research, The University of Western Australia, 35 Stirling Highway, Crawley, WA 6009, Australia*
[2]*School of Physics and Astronomy, University of St Andrews, North Haugh, St Andrews KY16 9SS, UK*

ABSTRACT

We present a consistent total flux catalogue for a $\sim$1 deg^2 subset of the Cosmic Evolution Survey (COSMOS) region (RA $\in$ [149°.55, 150°.65], Dec. $\in$ [1°.80, 2°.73]) with near-complete coverage in 38 bands from the far-ultraviolet to the far-infrared. We produce aperture matched photometry for 128 304 objects with $i < 24.5$ in a manner that is equivalent to the Wright et al. catalogue from the low-redshift ($z < 0.4$) Galaxy and Mass Assembly (GAMA) survey. This catalogue is based on publicly available imaging from *GALEX*, Canada–France–Hawaii Telescope, Subaru, Visible and Infrared Survey Telescope for Astronomy, *Spitzer* and *Herschel*, contains a robust total flux measurement or upper limit for every object in every waveband and complements our re-reduction of publicly available spectra in the same region. We perform a number of consistency checks, demonstrating that our catalogue is comparable to existing data sets, including the recent COSMOS2015 catalogue. We also release an updated Davies et al. spectroscopic catalogue that folds in new spectroscopic and photometric redshift data sets. The catalogues are available for download at http://cutout.icrar.org/G10/dataRelease.php. Our analysis is optimised for both panchromatic analysis over the full wavelength range and for direct comparison to GAMA, thus permitting measurements of galaxy evolution for $0 < z < 1$ while minimizing the systematic error resulting from disparate data reduction methods.

Key words: catalogues – galaxies: general – galaxies: photometry.

1 INTRODUCTION

Wide-area multiwavelength surveys such as the Sloan Digital Sky Survey (SDSS; York et al. 2000) and the UK Infrared Telescope Deep Sky Survey (Lawrence et al. 2007) have enabled the study of large, statistical samples of galaxies. However, such surveys are generally limited to low redshifts ($z < 0.3$), a single facility, and one region of the electromagnetic spectrum – usually the ultraviolet (UV), optical or near-infrared (IR). To produce a comprehensive picture of galaxy evolution, one must observe galaxies over an extensive range of wavelengths to probe multiple physical properties. This requires the combination of multiple data sets across observatories and instruments, and thus the consolidation of disparate sensitivities, resolutions and data reduction techniques (see e.g. Driver et al. 2016b).

Obtaining a consistent, optically motivated photometric catalogue for large multiwavelength data sets is highly non-trivial (Laidler et al. 2007; Wright et al. 2016). Naively position matching existing catalogues gives rise to the possibility of table mismatches,

especially when joining high-resolution (resolution $\sim$0.8 arcsec) optical data to low-resolution far-IR data (resolution $\sim$18 arcsec). Disparate data reduction methods, even though they may represent the most appropriate photometry in each individual band, may use differently sized and shaped apertures for the same object and hence probe different physical scales. More subtly, the different means of calculating errors by different survey teams will affect the quality of spectral energy distribution (SED) fits for a particular galaxy. Wright et al. (2016) show that the use of a multiwavelength catalogue derived using the same data reduction procedure across the full wavelength range results in reduced photometric inconsistency, and improves the accuracy of SED fits and star formation rate estimators compared to an equivalent catalogue constructed from table matching alone.

One technique to construct a consistent multiwavelength catalogue is a variation of (forced) matched aperture photometry, proceeding initially with aperture definition on a high-resolution image. The apertures are then propagated to the lower resolution data after convolution with the point spread function (PSF) and appropriate deblending. Software packages implementing this technique include TFIT (Laidler et al. 2007) and the Lambda-Adaptive Multi-Band Deblending Algorithm in R (LAMBDAR; Wright et al. 2016).

*⋆E-mail: stephen.andrews@icrar.org

One data set that lends itself to the construction of such a catalogue is the Galaxy and Mass Assembly (GAMA; Driver et al. 2011; Liske et al. 2015) survey. GAMA is a highly complete low-redshift spectroscopic and multiwavelength imaging campaign that aims to characterize the distribution of energy, mass and structure from kiloparsec to megaparsec scales. The GAMA spectroscopic campaign targeted 230° of sky using the AAOmega spectrograph on the 3.9 m Anglo-Australian Telescope, obtaining redshifts for ~250 000 galaxies. This spectroscopy is complemented by UV imaging from the *GALaxy Evolution eXplorer* (*GALEX*; Martin et al. 2005), optical imaging from SDSS and the Kilo-Degree Survey (de Jong et al. 2015), near-IR imagery from the VISTA (Visible and Infrared Survey Telescope for Astronomy) Kilo-degree Infrared Galaxy (Edge et al. 2013) survey, mid-IR imagery from the *Wide-field Infrared Survey Explorer* (Wright et al. 2010) and far-IR imagery from *Herschel*-Atlas (Eales et al. 2010) – see the summary in Driver et al. (2016b). The project has examined a wide variety of topics, including the cosmic SED (e.g. Driver et al. 2012, Andrews et al., in preparation), star formation rates (Davies et al. 2016a), large-scale structure (e.g. Alpaslan et al. 2014), galaxy groups (e.g. Robotham et al. 2011), close pairs (e.g. Davies et al. 2015b, 2016b) and galaxy properties and structure (e.g. Taylor et al. 2011; Kelvin et al. 2012; Loveday et al. 2015; Moffett et al. 2016). The GAMA survey, while scientifically comprehensive, by design, only probes the low-redshift Universe ($z < 0.4$). It is therefore beneficial that an intermediate redshift ($0.3 < z < 1$) equivalent to GAMA is established in order to explore a broader time baseline.

The Cosmological Evolution Survey (COSMOS; Scoville et al. 2007) region, covering 2 deg^2 of sky centred on RA = $10^\mathrm{h}00^\mathrm{m}28\overset{\mathrm{s}}{.}6$, Dec. = $+02°12'21\overset{''}{.}0$ is suitable for this purpose. The programme is anchored by F814W observations of the field using the *Hubble Space Telescope* (*HST*) and has been expanded to include deep observations spanning from X-ray wavelengths to radio – with observations conducted and released using *Chandra*, *GALEX*, the Canada–France–Hawaii Telescope (CFHT), Subaru, VISTA, *Spitzer* and *Herschel*. Spectroscopic surveys in the COSMOS region include zCOSMOS (Lilly et al. 2007, 2009), the PRIsm MUlti-object Survey (PRIMUS; Coil et al. 2011; Cool et al. 2013), the VISible Multi-Object Spectrograph (VIMOS)-Very Large Telescope (VLT) Deep Survey (VVDS; Garilli et al. 2008), the VIMOS Ultra Deep spectroscopic survey (Le Févre et al. 2015), the FMOS-COSMOS survey (Silverman et al. 2015), 3D-*HST* (Brammer et al. 2012) and SDSS DR10 (Ahn et al. 2014), complemented by large catalogues of photometric redshifts (Ilbert et al. 2009; Muzzin et al. 2013; Laigle et al. 2016). COSMOS has been used to study many aspects of galaxy formation and evolution, including the evolution of specific star formation rates (e.g. Ilbert et al. 2015), effects of environment on galaxy morphology (e.g. Capak et al. 2007b), high-redshift quasars (e.g. Masters et al. 2012) and dust-obscured galaxies (e.g. Riguccini et al. 2015). However, the multiwavelength data set was processed with different flux measurements and reduction methods resulting in a corresponding increase in systematic error.

Here, we construct a catalogue of consistent total flux measurements spanning from the far-ultraviolet (FUV) to the far-IR for a subregion we shall refer to as G10 and based on existing COSMOS imagery. Our catalogue, when combined with the spectroscopic redshifts crated by Davies et al. (2015a), forms an intermediate redshift sample prepared in an identical way to and thus suitable for direct comparison to GAMA. The combined multiwavelength data set is able to sample multiple processes occurring in the galaxy population across $0 < z < 1$, including (rest frame) UV light from star

formation, optical and near-IR emission from young and old stars, mid-IR emission from polycyclic aromatic hydrocarbons and warm dust (50 K), and far-IR emission from cold dust (20 K). In Section 2, we describe the multiwavelength data set used. In Section 3, we construct a consistent 38 band photometric catalogue spanning the FUV to the far-IR in a subset of the COSMOS region using LAMBDAR. In Section 4, we demonstrate consistency with existing photometric catalogues in the region. Sections 5 and 6 summarize the release content and present concluding remarks, respectively. In four upcoming papers, we use this data in conjunction with GAMA to examine stellar and dust masses (Driver et al., in preparation; Wright et al., in preparation), the cosmic SED (Andrews et al., in preparation) and star formation rates (Davies et al., in preparation).

We use AB magnitudes throughout this work.

2 DATA

In this section, we describe the imaging and redshift information used to construct our multiwavelength catalogue and their respective surveys. Fig. 1 shows the combination of 22 broad-band filters used in these surveys (omitting B, V and the intermediate- and narrow-bands for clarity). Also shown, for illustrative purposes only, is the Driver et al. (2012) cosmic SED redshifted to $z = 0.5$ to highlight the emission from a typical galaxy (barring evolution that will be examined in a later study). The 5σ point source detection thresholds of these data sets, as computed from the median sky rms for 1000 random sources, are shown in Fig. 2.

2.1 GAMA G10

To provide an intermediate redshift comparison for the GAMA project, Davies et al. (2015a) re-reduced spectra from zCOSMOS (Lilly et al. 2007, 2009) and combined them with spectroscopic redshifts from other surveys, obtaining redshifts for over 22 000 sources. The 'bright' component of zCOSMOS targeted 20 000 sources closer than $z < 1.2$ using the VIMOS on the VLT. The zCOSMOS observations used a slit length of 10 arcsec that raises the possibility of confusion in dense regions.

The zCOSMOS-bright raw spectra were re-reduced using a bespoke pipeline, fitted using AUTOZ (Baldry et al. 2014) and position matched to a reverse engineered version of the non-public zCOSMOS input catalogue. The mismatch rate between the original catalogue and the reverse-engineered catalogue is estimated to be 2 per cent.

Both the AUTOZ and original zCOSMOS redshifts were then combined with spectroscopic redshifts from PRIMUS, VVDS and SDSS and photometric redshifts from Ilbert et al. (2009), and matched to the broader COSMOS photometric catalogue. As a result of this combination, each source in the COSMOS catalogue is automatically assigned both a 'best' redshift (Z_BEST) and a reliability flag (Z_USE) – Z_USE = 1 indicates high-resolution, reliable spectroscopic redshifts and Z_USE < 3 represents reliable spectroscopic redshifts. Spectra for all zCOSMOS targeted sources were then visually inspected with the redshift and reliability flag adjusted accordingly.

The G10 region (RA $\in$ [149°.55, 150°.65], Dec. $\in$ [1.80, 2°.73]) is a subset of the COSMOS region chosen for its relatively high spectroscopic completeness of ~45 per cent for extragalactic sources with $i < 22$ mag. This spectroscopic completeness is shown in Fig. 3. The G10 region has full multiwavelength coverage except for the Ultra-VISTA bands (0.25 per cent missing). This work uses the second
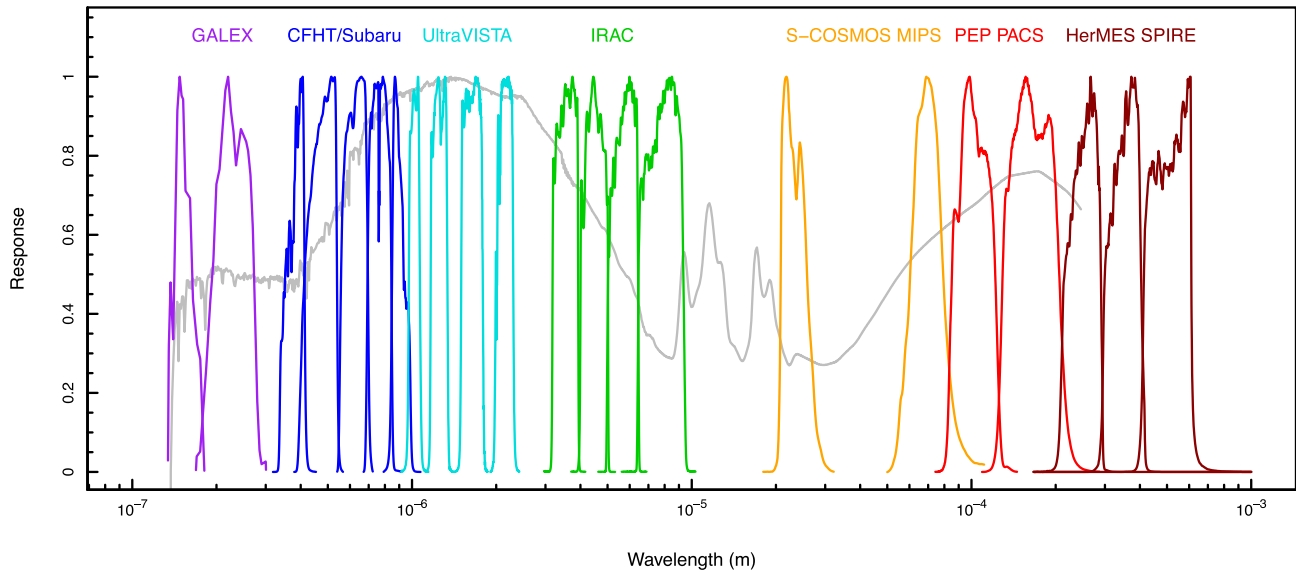
Figure 1. The combined broad-band filter curves of this multiwavelength data set, colour-coded by survey and normalized to 1. Subaru B, V and the intermediate and narrow-bands are omitted for clarity. In grey is the Driver et al. (2012) cosmic spectral energy distribution redshifted to $z = 0.5$ to illustrate what the energy-weighted average galaxy spectral energy distribution may look like at this redshift.
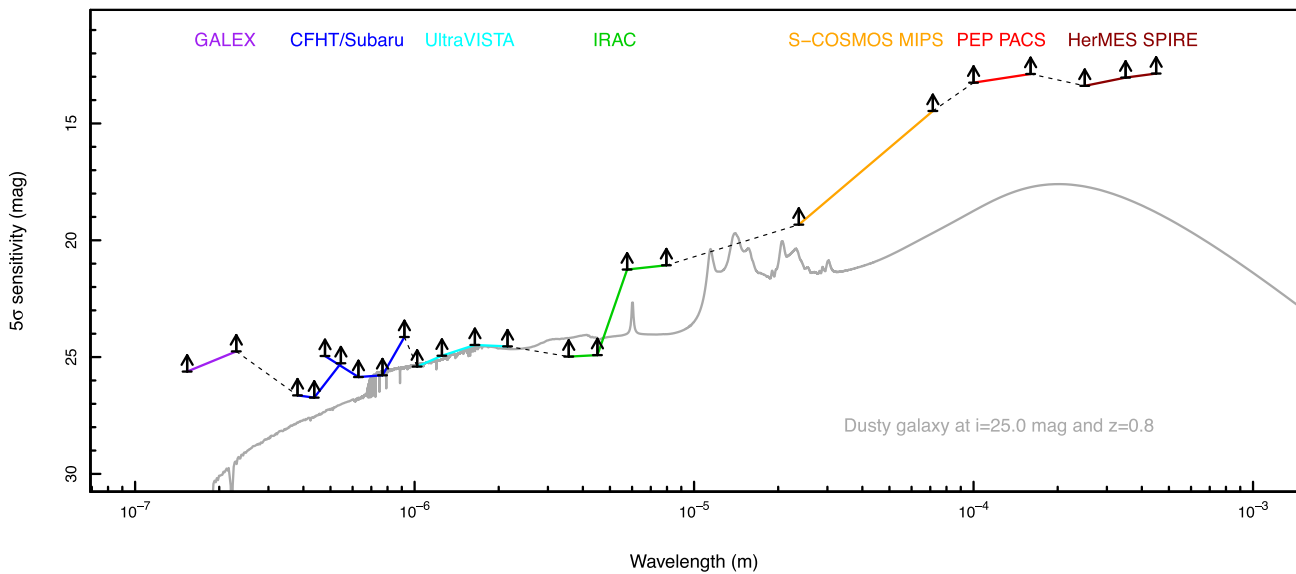

Figure 2. The 5σ limit for point sources of the different multiwavelength components as computed from the median sky RMS for 1000 random sources in the respective bands for the broad-band filters. The grey curve is an example SED fit of a dusty galaxy, scaled to $i = 25$ mag and redshifted to $z = 0.8$.

version of the Davies et al. (2015a) catalogue, G10CosmosCatv02, as described in Section 5.[1]

2.2 COSMOS

As part of the COSMOS multiwavelength imaging campaign, Capak et al. (2007a) and Taniguchi et al. (2007, 2015) obtained imagery from the 8.3 m Subaru telecope in *BgVriz* and 14 narrow and intermediate bands and the 3.6 m CFHT in the *ui* bands. Both telescopes are situated on Mauna Kea, Hawaii.

The Subaru imaging was obtained using Suprime-Cam (Komiyama et al. 2003) in 2004 and 2005 with exposure times ranged from 5.8 to 10.8 h. Suprime-Cam is an array of 10 2048 × 4096 CCDs with a 34 arcmin × 27 arcmin field of view and native resolution of 0.202 arcsec pixel^{-1}. Worst case seeing for the Subaru data ranged from 0.95 arcsec in B and i to 1.58 arcsec in g. Taniguchi et al. (2007) claims 90 per cent completeness in *BgVriz* for exponential disc galaxies down to 24.7, 24.3, 24.1, 24.1, 23.5 and 22.9 mag, respectively. A follow-up survey in 2006 and 2007 (presented by Taniguchi et al. 2015) added imagery in 13 intermediate- and narrow-band filters.

The CFHT images were obtained using the Mega-Prime camera (Aune et al. 2003; Boulade et al. 2003) from 2003 December to 2005 June and combined using SWARP (Bertin et al. 2002).
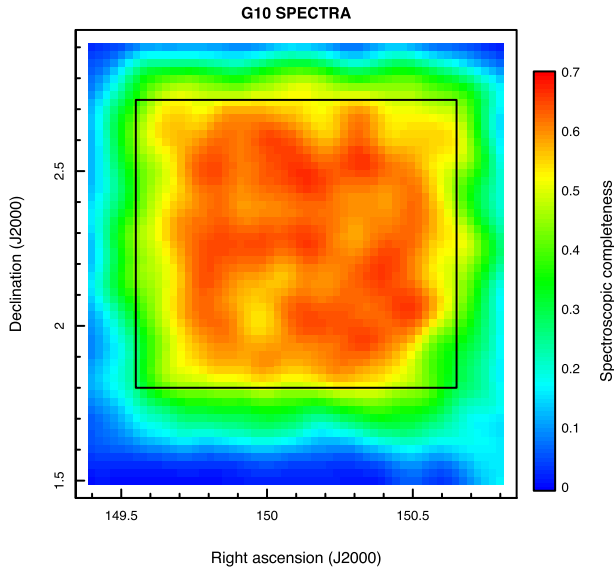
[1] http://cutout.icrar.org/G10/dataRelease.php

Figure 3. Spectroscopic completeness of the COSMOS field for $i < 22.0$ mag on 1.5 arcmin scales. The G10 region is denoted by the black box.

Mega-Prime is an array of 36 2 K × 4.5 K EEV CCDs with a 1 deg² field of view with a native resolution of 0.18 arcsec pixel⁻¹. The worst case seeing was 0.9 arcsec in *u* and 0.94 arcsec in *i* and the 5σ limiting magnitude for a 3 arcsec circular aperture was 26.5 mag in *u* and 23.5 mag in *i*.

Images from both telescopes were resampled to a common resolution of 0.15 arcsec pixel⁻¹ and aligned on to a common astrometric grid by the COSMOS collaboration. This work uses the original PSF (Subaru version 2) mosaics for all bands[2] except CFHT *u* that contains a zero-point error. In this case, we assembled a mosaic covering the entire COSMOS region from the individual original PSF (CFHT version 5) tiles available on the COSMOS archive[3] using SWARP.

2.3 *GALEX*

The COSMOS region was observed using the *GALEX* as part of the Deep Imaging Survey (Zamojski et al. 2007).[4] *GALEX* was an UV space observatory operated by NASA, launched on 2003 April 28 and decommissioned on 2013 June 28. The observatory was equipped with a 0.5 m mirror, a circular field of view 1°.2 in diameter, a 1.5 arcsec pixel⁻¹ detector and two passbands in the far- and near-ultraviolet (FUV and NUV), respectively. Observations consisted of four pointings with exposure times of 45 000 s in FUV with a PSF full width at half-maximum (FWHM) of 5.4 arcsec and 50 000 s in NUV with a PSF FWHM of 5.6 arcsec. We assembled the four *GALEX* (version 2) pointings for each band into a single mosaic using SWARP with background subtraction turned off.

2.4 UltraVISTA

The near-IR UltraVISTA survey (McCracken et al. 2012) is currently being conducted on the VISTA using the VISTA Infrared

Camera (VIRCAM). VISTA is a 4 m telescope operated by the European Southern Observatory (ESO) in Paranal, Chile. VIRCAM is an array of 16 Raytheon 2048 Å – 2048 detectors with a native resolution of 0.339 arcsec pixel⁻¹.

This work uses the second UltraVISTA data release[5] that surveyed the COSMOS region during 2009 December–2012 May in the *YJHK$_s$* wideband filterset for at least 11.1, 12.8, 13.3 and 10.6 h. The typical PSF FWHM was 0.9 arcsec across all four bands. UltraVISTA is composed of two components – Deep and Ultra-deep surveys – outlaid on the sky in alternating vertical stripes ∼0°.2 wide in RA. The Deep survey claims limiting magnitudes of 25.1, 24.8, 24.4 and 24.5 mag in *YJHK$_s$*, while the Ultra-deep survey (as of DR2) claims limiting magnitudes of 25.7, 25.4, 25.0, 24.8 mag, respectively. A small portion of the G10 region near RA = 150°.55, Dec. = 1°.83 has no data in any UltraVISTA band due to a faulty detector (see Fig. 4). UltraVISTA DR2 images have been resampled to a pixel scale of 0.15 arcsec pixel⁻¹ and aligned to the COSMOS astrometric grid by the UltraVISTA collaboration.

2.5 S-COSMOS and SPLASH

The COSMOS *Spitzer* survey (S-COSMOS; Sanders et al. 2007) surveyed the COSMOS region using the *Spitzer Space Telescope*. *Spitzer* is a 0.85 m mid-IR space observatory operated by NASA launched on 2003 August 25. S-COSMOS observed in all passbands of the Infrared Array Camera (IRAC) and the Multiband Imaging Photometer for *Spitzer* (MIPS). After exhaustion of the cryogen on 2009 May 15, only the two shortest wavelength IRAC passbands are operational.

IRAC is a set of two 256 × 256 pixels detectors with four filters centred on 3.6, 4.5, 5.6, 8.0 μm referred to as bands 1–4, respectively. IRAC has a native pixel resolution of 1.2 arcsec pixel⁻¹ and field of view of 5.2 arcmin × 5.2 arcmin. IRAC G03 observations of the COSMOS region have a typical exposure time of 1200–2200 s and PSF FWHMs of 1.7, 1.7, 1.9 and 2.0 arcsec in bands 1–4, respectively.

During the *Spitzer* warm mission, the *Spitzer* Large Area Survey with Hyper-Suprime-Cam (SPLASH; Capak et al., in preparation) surveyed the COSMOS field with a typical exposure time of 3.8 h per pixel in IRAC channels 1 and 2. These observations achieved a 5σ depth of 0.2 μJy, compared to 0.9 μJy for S-COSMOS. The released images have been resampled to 0.6 arcsec pixel⁻¹ by the S-COSMOS and SPLASH collaborations.

MIPS was a set of three detector arrays with 128 × 128, 32 × 32 and 2 × 2 pixels with a pixel scale of 1.2, 4.0 and 8.0 arcsec pixel⁻¹ at 24, 70, and 160 μm, respectively. The G03 MIPS observations of COSMOS took place during 2006 January–2008 January. Integration times were 2800, 1350 and 270 s and PSF FWHMs were 5.9, 18.6 and 39 arcsec for 24.0, 70.0, and 160.0 μm, respectively. The 1σ noise level was 1.7 and 13 mJy in 70 and 160 μm. The MIPS 70 and 160 μm observation strategy and data reduction process is described in Frayer et al. (2009) and the MIPS 24 catalogue is briefly described in Le Floc'h et al. (2009).

This work uses all SPLASH data and MIPS observations at 24 (version 1) and 70 μm (version 3).[6] We do not adopt the MIPS 160 data as *Herschel* data offer superior sensitivity and resolution.

---

[2] https://irsa.ipac.caltech.edu/data/COSMOS/images/subaru/
[3] https://irsa.ipac.caltech.edu/data/COSMOS/images/cfht/
[4] https://irsa.ipac.caltech.edu/data/COSMOS/images/galex/

[5] http://ultravista.org/DR2
[6] https://irsa.ipac.caltech.edu/data/COSMOS/images/spitzer/mips/

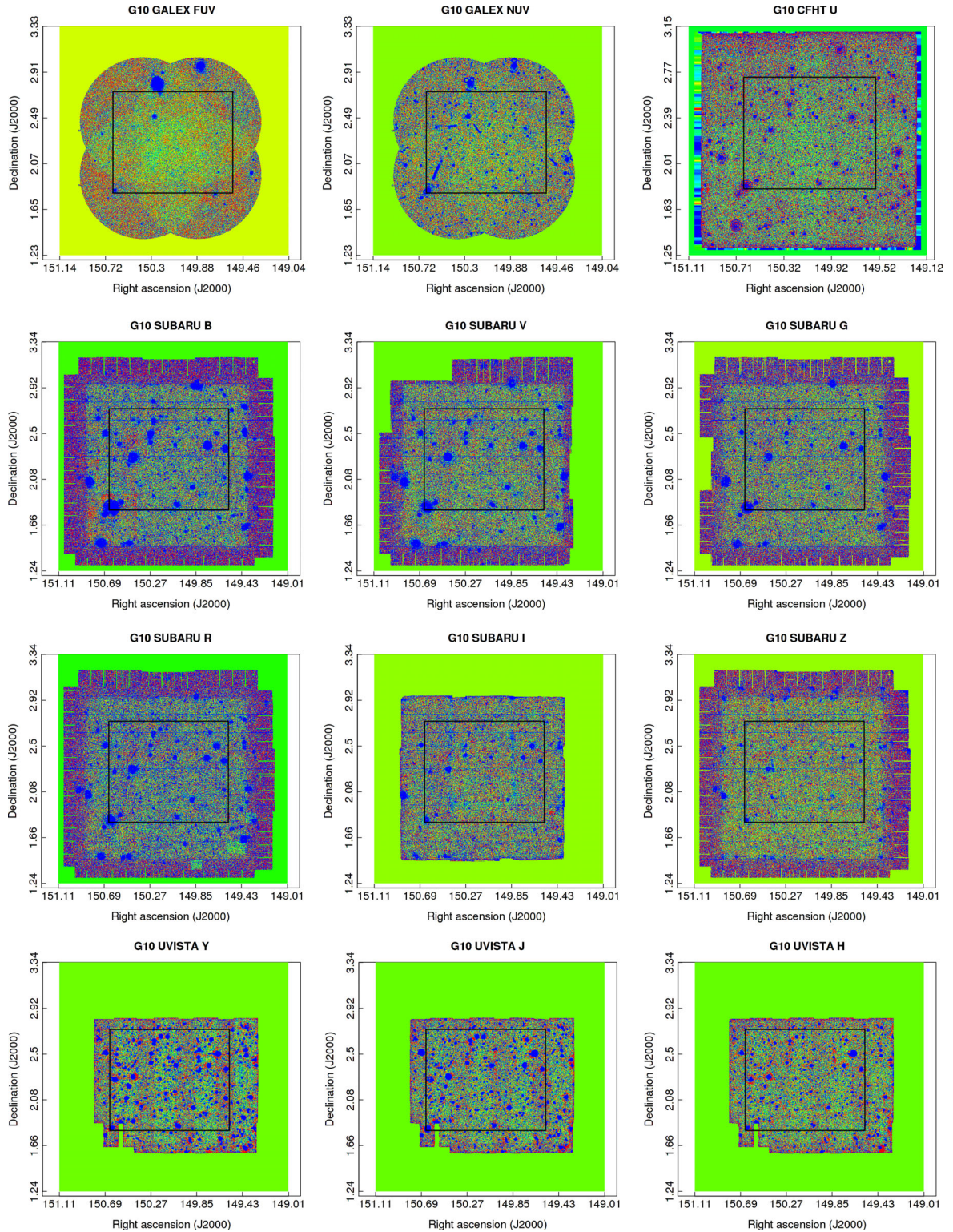**Figure 4.** Background uniformity and coverage for the *GALEX*, COSMOS, UltraVISTA, S-COSMOS, PEP and HerMES data. The black box denotes the G10 region. Resolution has been reduced to 1.5 arcsec per pixel and levels adjusted to be close to the sky noise.

2.6 PACS evolutionary probe

The PACS (Photodetector Array Camera and Spectrometer) Evolutionary Probe (PEP; Lutz et al. 2011) was a survey conducted on the *Herschel space observatory*. *Herschel* (Pilbratt et al. 2010) was a 3.5 m far-IR space telescope operated by the European Space Agency from launch on 2009 May 14–2013 April 29, when the cryogenic coolant was exhausted.

PACS (Poglitsch et al. 2010) was a combined imagery and integral field spectroscopy instrument whose two 16×25 pixel bolometer arrays had pixel scales of 1.2 and 2.4 arcsec pixel^{-1} and a field
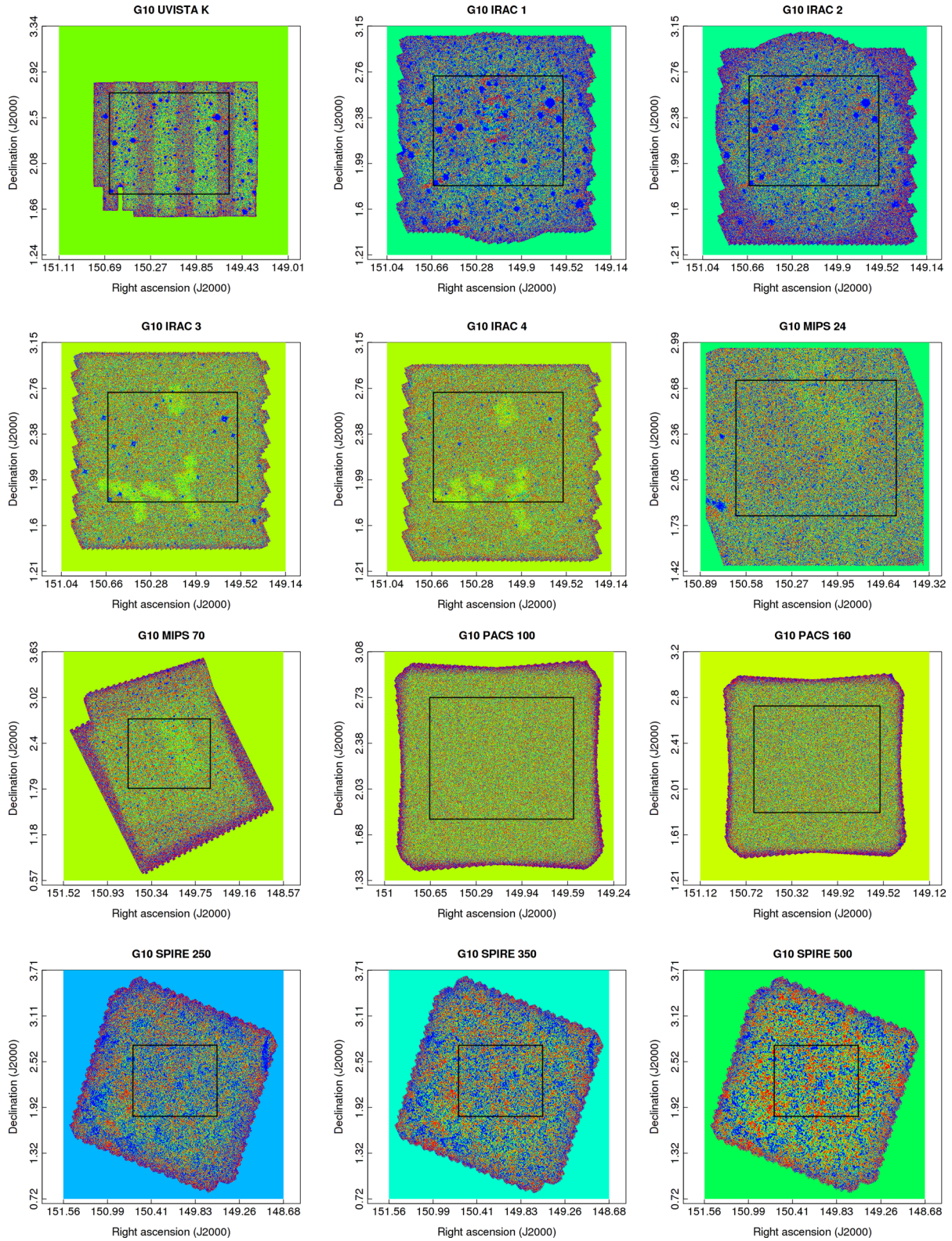
Figure 4 – *continued*

of view of 1.75 arcmin × 3.5 arcmin. The instrument featured passbands centred around 70, 100 (1.2 arcsec pixel^{-1}) and 160 μm (2.4 arcsec pixel^{-1}).

This work uses the first PEP data release.[7] PEP surveyed the COSMOS region at 100 and 160 μm for 196.9 h in the period 2009 November–2010 June, yielding images with PSF FWHM of 7.4 and 11.3 arcsec at 100 and 160 μm, respectively. The observations achieved a confusion-limited 3σ sensitivity at 160 μm of 10.2 mJy.

2.7 HerMES

The *Herschel* Multi-Tiered Extragalactic Survey (HerMES; Oliver et al. 2012) was a far-IR survey conducted on the *Herschel space observatory* using the Spectral and Photometric Imaging Receiver (SPIRE). SPIRE (Griffin et al. 2010) was a combined three-band imager and Fourier-transform spectrometer with a 4 arcmin × 8 arcmin field of view. The imaging bands were centred on approximately 250, 350 and 500 μm with pixel scale 6.0, 8.3 and 12.0 arcsec pixel^{-1} and FWHM of 18.15, 25.15 and 36.3 arcsec, respectively.

This work uses the second HerMES data release.[8] HerMES surveyed the COSMOS region in the three SPIRE bands for approximately 50 h, achieving a 5σ noise limit of 8.0, 6.6 and 9.6 mJy in 250, 350 and 500 μm, respectively. The reduction process for the HerMES images is described in Levenson et al. (2010) and Viero et al. (2013) and the construction of the HerMES catalogues is described in Roseboom et al. (2010), Smith et al. (2012) and Wang et al. (2014).

2.8 Characteristics of the multiwavelength data set

Fig. 4 presents an overview of the coverage and background properties of the multiwavelength data set. Images were resampled to 1.5 arcsec per pixel using SWARP and levels adjusted to be close to the sky background (±2σ) using MOGRIFY. At these scales, astronomical objects are not visible. The circular 'holes' in wavelengths shorter than IRAC 4 are haloes of faint light surrounding saturated stars. The four circular pointings of *GALEX* and the alternating deep and Ultra-Deep stripes of UltraVISTA are both clearly visible. Also visible are window and dichroic reflections (rings) and bevel reflections (streaks) in the *GALEX* NUV data. The non-uniform background seen in the HerMES data is a result of Galactic cirrus.

Both the G10 catalogue and a cutout generator for the multiwavelength imagery described above are available at http://cutout.icrar.org/G10/dataRelease.php. Some key details of the multiwavelength imagery are outlined in Table 1.

3 PHOTOMETRY

3.1 Existing photometry in the G10 region

Existing photometry in the COSMOS region consists of an assortment of independent flux measurements and data reduction methods. For instance, the Capak et al. (2007a) optical COSMOS photometric catalogue provides an AUTO flux measurement in only the Subaru *i* band and fixed 3 arcsec apertures for all Subaru and CFHT bands, UltraVISTA provides SEXTRACTOR (Bertin & Arnouts 1996) derived AUTO magnitudes for all four near-IR bands and

S-COSMOS provides a catalogue of four different flux measurements using fixed-sized apertures (1.4, 1.9, 2.9 and 4.1 arcsec) in the IRAC bands. Muzzin et al. (2013) homogenizes this data set, but they calculate 2.1 arcsec fixed-size apertures and do not include the *Herschel* data.

Inhomogeneous analytical techniques and the use of fixed-size apertures can potentially introduce systematic and random errors for a subset of scientific investigations such as measuring the cosmic SED at intermediate redshifts. Fig. 6 shows that the 2 and 3 arcsec apertures used by the COSMOS 2007 (now obsolete) catalogue are unsuitable for objects at low to intermediate redshifts. 3 arcsec apertures are also unsuitably large for the region depicted in the right-hand panel.

Recently, the COSMOS2015 catalogue (Laigle et al. 2016) derived fixed-size and AUTO aperture photometric measurements for sources originally detected on a *zYJHK* co-added image. Aperture definitions were propagated to PSF-matched images from *u* through *K* using SEXTRACTOR's dual image mode. The catalogue also contains existing photometry from *GALEX*, updated photometry from IRAC derived using IRACLEAN (Hsieh et al. 2012), updated MIPS photometry and *Herschel* photometry based on MIPS 24 μm priors, but does not include MIPS 70 or *g*.

While the COSMOS2015 catalogue provides exquisite PSF matched photometry from *u* − *K*, the full panchromatic grasp is obtained from table matching with previously constructed *GALEX* and *Herschel* catalogues. For the purpose of full SED modelling table matching, as opposed to 'forced' photometry can introduce unphysical discontinuities at the wavelength interfaces. In SED modelling, a consistent measurement and even more importantly, a consistent error assessment across the full wavelength range is critical. Whether such issues are relevant can only be established after conducting a fully panchromatic analysis and comparing the outcome. To that extent, the aim of this paper is to re-define a set of detections and apertures and derive consistent, total flux photometry in the G10 region using LAMBDAR, specifically for panchromatic analysis over the entire wavelength range. This also permits direct comparisons with the LAMBDAR-derived photometry of low-redshift sources from GAMA (Wright et al. 2016).

3.2 LAMBDAR

We use LAMBDAR (Wright et al. 2016)[9] to construct reliable panchromatic photometry for the G10 region across all bands outlined in Section 2. LAMBDAR is explicitly designed to deal with the resolution mismatch that arises from multiwavelength data sets, and deblending that is capable of dealing with low resolution and confused far-IR data.

Briefly, LAMBDAR requires a set of aperture definitions (RA, Dec., semimajor and semiminor axes and position angle) and a set of input images. Input images do not have to be pixel-matched nor astrometrically aligned. The input apertures must be robust – the shredding depicted in the left-hand and centre panels of Fig. 6 (regardless of the use of fixed-sized apertures) will lead to the flux being significantly underestimated, while the incorrect apertures in the right-hand panel of Fig. 6 would cause flux to be erroneously large for the faint central objects and erroneously small for the surrounding bright objects and objects on the edge of the complex. The user can also supply a list of contaminants – objects with defined

---

Table 1. Band-dependant LAMBDAR settings and image metadata.

Band	PSF FWHM (arcsec)	Zeropoint (mag)	Saturation (counts)	Pixel size (arcsec)	Saturation value (counts)
FUV	See Section 3.4	18.82	–	1.5	–
NUV	See Section 3.4	20.08	–	1.5	–
u	0.9	31.4	5538	0.15	–
B	0.95	31.4	2645	0.15	6501
V	1.33	31.4	1350	0.15	5301
g	1.58	31.4	1516	0.15	3601
r	1.05	31.4	2166	0.15	5501
i	0.95	31.4	799	0.15	3001
z	1.15	31.4	1805	0.15	6401
IA427	1.64	31.4	–	0.15	45 001
IA464	1.89	31.4	–	0.15	37 001
IA484	1.14	31.4	–	0.15	39 601
IA505	1.44	31.4	–	0.15	41 701
IA527	1.60	31.4	–	0.15	31 301
IA574	1.71	31.4	–	0.15	21 701
IA624	1.05	31.4	–	0.15	28 501
IA679	1.58	31.4	–	0.15	32 201
IA709	1.58	31.4	–	0.15	21 901
IA738	1.09	31.4	–	0.15	28 601
IA767	1.65	31.4	–	0.15	21 401
IA827	1.74	31.4	–	0.15	22 701
NB711	0.79	31.4	1200	0.15	141 701
NB816	1.51	31.4	5495	0.15	58 301
Y	0.9	30.0	24 516	0.15	–
J	0.9	30.0	24 516	0.15	–
H	0.9	30.0	24 516	0.15	–
K	0.9	30.0	24 516	0.15	–
i1	See Section 3.4	21.58	–	0.6	–
i2	See Section 3.4	21.58	–	0.6	–
i3	See Section 3.4	21.58	–	0.6	–
i4	See Section 3.4	21.58	–	0.6	–
m24	See Section 3.4	20.15	–	1.2	–
m70	See Section 3.4	17.53	–	4.0	–
p100	See Section 3.4	8.9	–	1.2	–
p160	See Section 3.4	8.9	–	2.4	–
s250	18.15	8.9	–	6.0	–
s350	25.15	8.9	–	8.3	–
s500	36.3	8.9	–	12.0	–

apertures that are fully deblended using the following method, but without flux measurements being performed.

For each image, LAMBDAR optionally convolves input apertures with the PSF, giving an aperture function $A_i(x, y)$ for each object. The PSF may be integrated outwards to encapsulate some fraction of the total integral (parameter name `PSFConfidence`) and truncated at the corresponding radius. The normalization of the aperture functions can be scaled by a set of prior flux weights w_i either supplied by the user or determined using the flux of the central pixel. LAMBDAR then calculates the deblend function

$$D_i(x, y) = \frac{w_i A_i(x, y)}{\sum_i w_i A(x, y)}, \qquad (1)$$

for each object, which is the ratio of the weighted aperture function of the object to the sum of all weighted aperture functions for a particular pixel. The deblended image, i.e. the product of $D_i(x, y)$ and the image $I(x, y)$, governs how much flux is assigned to object i. LAMBDAR then performs either PSF-weighted photometry – that multiplies the deblended image by the aperture function – or aperture photometry that converts the aperture function into a simple aperture before multiplication. The latter is achieved by integrating

$A_i(x, y)$ outwards to some fraction of the total integral (`ApertureConfLimit`) and assigning $A(x, y) = 1$ or 0 accordingly. The process of flux determination may be repeated iteratively, with the output flux measurements being used as input weights. The program is also capable of performing local sky subtraction, blanks and randoms corrections. For full details of the LAMBDAR code, see Wright et al. (2016).

3.3 Input catalogue

As noted above, LAMBDAR does not perform blind source detection and aperture definition. To obtain the input apertures, we ran SEXTRACTOR (v2.19.5) on the i-band Subaru mosaic, with the saturated NaN regions replaced with a nominal value (3001) to avoid shredding of bright stars. After some trial and improvement, we use a detection threshold of 3σ, analysis threshold of 1.5σ, deblending parameters DEBLEND_NTHRESH = 64, DEBLEND_MINCONT = 0.0004 and no convolution filter. This provides the most qualitatively robust apertures, compromising between faint source detection, close source deblending and minimizing over deblending of large resolved sources. We find the
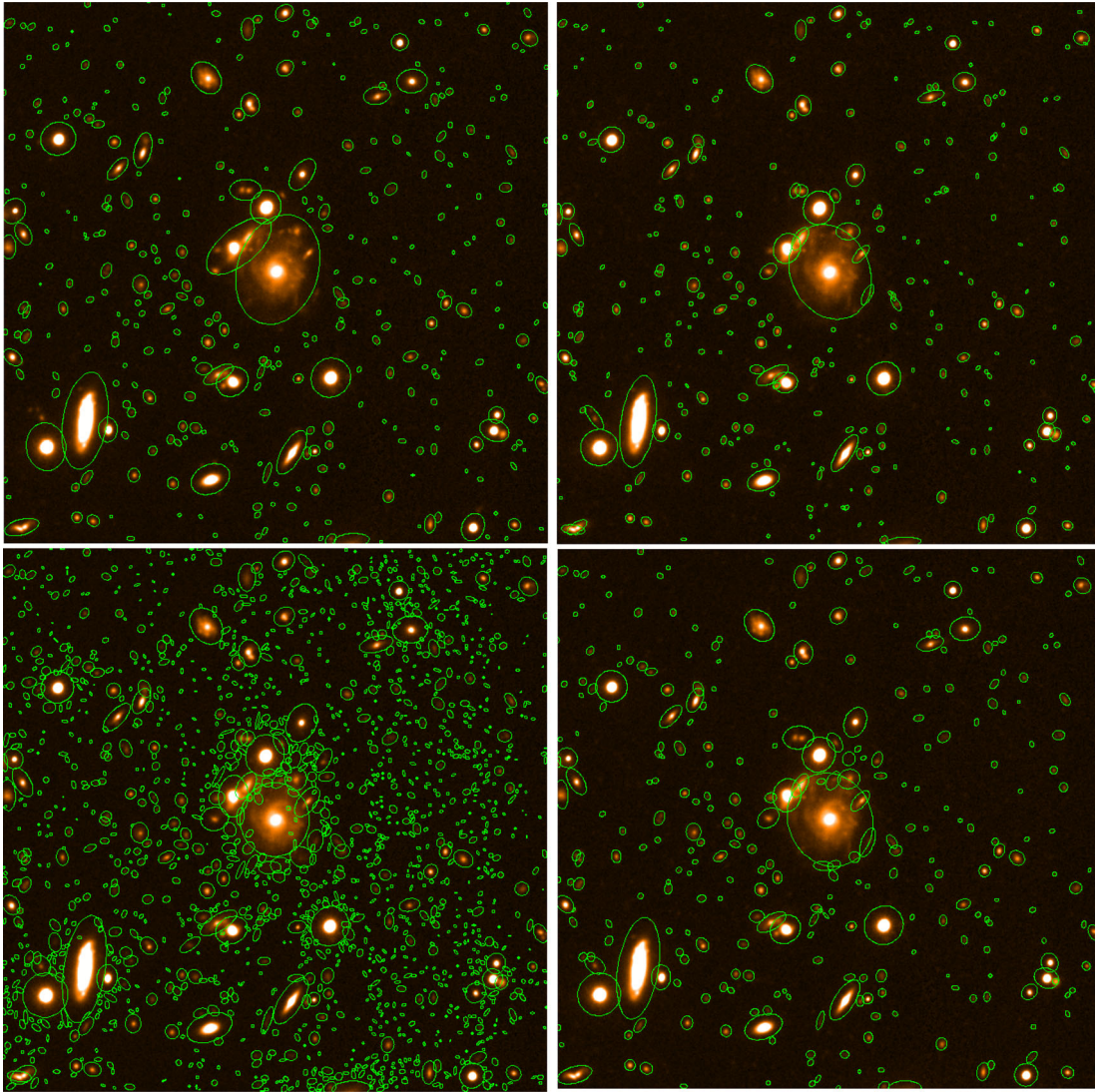
Figure 5. A sample region (50 arcsec × 50 arcsec) with apertures obtained using the SEXTRACTOR default settings (top left), the COSMOS settings optimized for their PSF-matched data (bottom left), the COSMOS2015 settings (bottom right) and our settings (top right). Particular improvement is seen in the deblending solution around the central object, achieving a result similar to COSMOS2015.

SEXTRACTOR default settings do not deblend sufficiently, while the Capak et al. (2007a) settings – that are tailored for the PSF-matched and stacked (CFHT and Subaru *i* band) image used for the construction of the COSMOS (2007, now obsolete) photometric catalogue – produce large amounts of false detections and shredded objects (a cut of *i* < 25 mag in total flux was applied to their public catalogue). The COSMOS2015 deblend solution produces similar results to ours. Fig. 5 compares our settings to both the default and COSMOS 2007 (bottom left) and 2015 (bottom right) settings for a small cutout.

Despite the above choice of parameters, Fig. 6 (middle panel) shows that problematic apertures still exist for large or flocculent galaxies and near bright objects. We use the aperture magnitude–size plane depicted in Fig. 7 to identify potentially bad apertures and objects prone to shredding. We then examined cutouts containing objects *i* < 25 mag that meet any of the following criteria: *i* < 18 mag, semimajor axis >6 arcsec, *i* + semimajor axis (in arcsec, see the lower diagonal line in Fig. 7) <22, *i* + semimajor axis (in arcsec, see the upper diagonal line in Fig. 7) >27.5 or a

positional offset between the input catalogue and COSMOS photometric catalogue of >0.5 arcsec. These cuts are shown in blue in Fig. 7. Apertures above and to the left of this region are either objects that did not deblend correctly or large, bright objects prone to shredding, while non-stellar sources below the region are the result of shredding. For objects that have redshift information, we also required Z_BEST > 0.01 and Z_USE < 5 (sources not flagged as stars). For objects that do not have a redshift measurement, we required objects brighter than *i* < 18 mag to have a semimajor axis >4 arcsec.

Of the 6547 (3.5 per cent of total) sources inspected, 2785 (1.5 per cent) required manual intervention, 651 (0.3 per cent) were false detections and 1838 (1.0 per cent) were replaced with point sources. Manual inspections were performed by SKA, LJMD and SPD and involved both fixing the primary aperture and fixing, adding or removing apertures down to *i* < 25 mag whose centre lies within 1.5 times the revised semimajor axis of the primary object. Inspections and fixes were performed using a bespoke interface written by ASGR using the SHINY framework. In addition, any
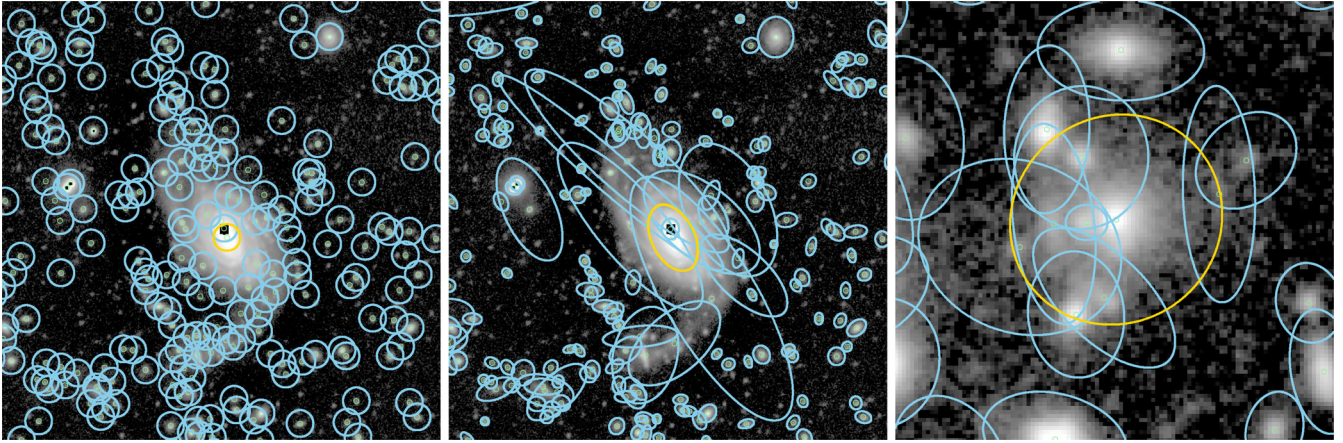
Figure 6. Subaru *i* band cutouts of CATAIDs 6008198 (left and centre, 50 arcsec radius) and 6002104 (right, 8 arcsec radius), denoted by the gold apertures. Left-hand panel: each source is associated with a 3 arcsec aperture and corresponds to an object in the G10/COSMOS photometric catalogue. The centre and right-hand panels show 6008198 and 6002104, respectively, but with aperture parameters derived from our catalogue prior to manual intervention. The saturated region corresponds to a foreground star.
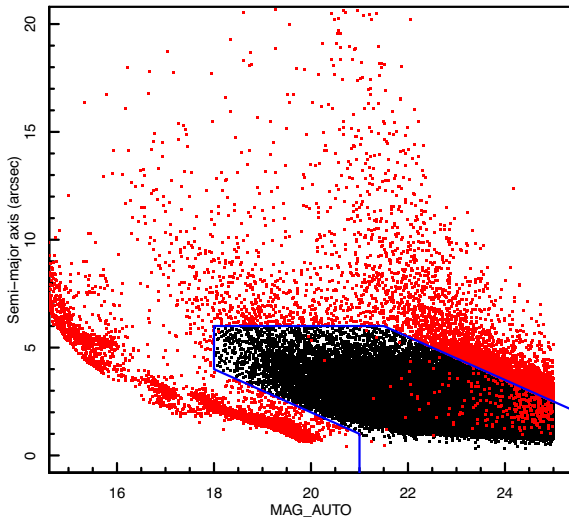

Figure 7. SEXTRACTOR-derived semimajor axis versus *i*-band magnitude for our sample. Apertures selected for inspection (red) either lie outside the blue lines (see the text), or have a positional offset of more than 0.5 arcsec compared to the COSMOS photometric catalogue. Objects outside the blue lines that are not selected for inspection are known spectroscopic stars.

Figure 8. Semimajor axis after aperture fixing versus *i*-band magnitude for our sample. Objects with changed apertures are denoted with green points.

apertures with a semimajor axis less than the Subaru *i* PSF FWHM of 0.95 arcsec were replaced with a point source.

However, the above procedure failed to recover the very brightest stars due to positional mismatch. To overcome this issue, we ran SEXTRACTOR on the CFHT *i*-band mosaic with default-like settings – varying only the detection threshold (3σ), sky background mesh size (512 pixels) and memory settings. We then position matched this catalogue to the G10/COSMOS catalogue to 1 arcsec and used the CFHT aperture parameters for CATAIDs brighter than $i < 19$ mag (as measured on the CFHT image) that were not manually inspected. This resulted in 2256 apertures (1.2 per cent) being updated.

Another potential issue is that apertures in regions requiring complex deblending were systematically larger than their constituent objects. One such example is presented in the right-hand panel of Fig. 6. To (partially) address this problem, we selected objects where the primary aperture has at least five overlapping apertures, or where the weighted sum of the overlapping areas are at least
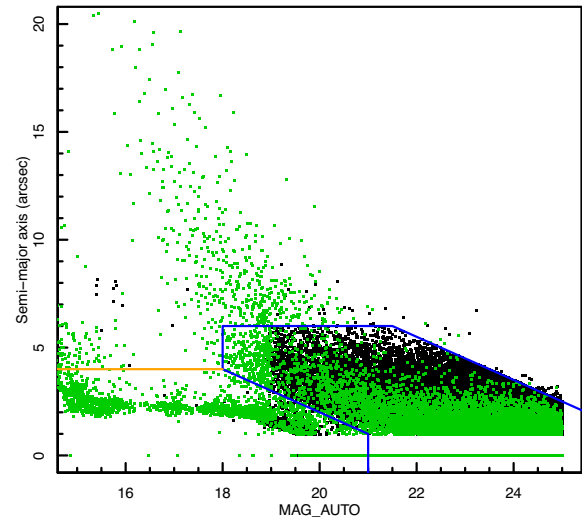
125 per cent of the area of the primary aperture (an area that is covered by *n* overlapping apertures is counted *n* times). We performed an internal match of this list to a 6 arcsec radius, then checked and fixed by eye objects within 6 arcsec or 1.5 times the semimajor axis of the primary object (whichever was larger). 1209 regions were fixed in this manner. The aperture catalogue and mosaic were then overlain on screen and visually inspected, with any obvious remaining problems fixed by hand.

In total, there are 185 907 objects in the G10 region, of which 17 062 (9.2 per cent) had apertures requiring manual inspection. This included manually fixing 2785 (1.5 per cent) sources, removing 651 (0.3 per cent) false detections, replacing 1838 (1.0 per cent) with point sources, adding 1722 objects (1.0 per cent) and fixing 1209 (0.7 per cent) regions manually. In this process, 9480 (5.1 per cent) neighbouring sources were also fixed. The resulting size–magnitude distribution, analogous to Fig. 7, is shown in Fig. 8 with the changed apertures denoted with green points. Fig. 9 is analogous to Fig. 6, but with the manual fixes incorporated. Manual inspections took
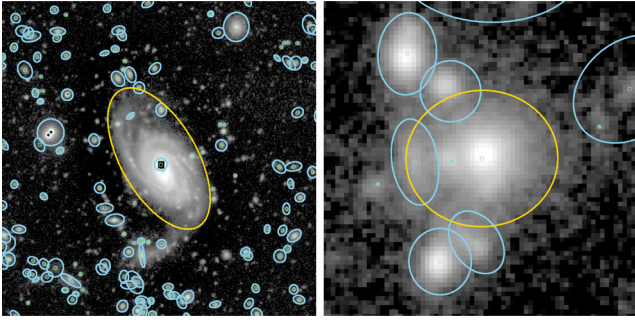
Figure 9. Subaru *i*-band cutout of GAMA objects 6008198 (left) and 6002104 (right) using the final aperture catalogue analogous to Fig. 6. A green dot without a corresponding aperture ellipse represents a point source.

about one minute each, with total time expended of the order of 100 person-hours.

The total number of objects fixed manually, and the number of potentially problematic apertures remaining, highlight the need for increasing the accuracy of automated aperture determination for the next generation of galaxy surveys, for example, the Wide Area VISTA Extragalactic Survey (WAVES; Driver et al. 2016a). These surveys have comparable source density to the COSMOS region but instead cover hundreds of square degrees, making manual intervention prohibitively labour intensive.

3.4 Obtaining photometry

In order to obtain robust matched aperture photometry in the G10 region, we ran LAMBDAR to obtain photometry for all objects with $i < 25$ mag. A contaminant list is not required in the optical and near-IR (NIR) because we are targeting all objects above a constant flux level. Again, we replaced all saturated regions in the Subaru imagery with a nominal value above the saturation threshold (see Table 1) equal to approximately 90 per cent of the maximum pixel value. This replacement also reduces artificial shredding of apertures. This causes somewhat incorrect photometry for bright, nearby and hence saturated objects, but is inconsequential because we are primarily focusing on fainter systems at intermediate redshifts. These objects are flagged in the individual band catalogues detailed in Section 5.

For the IRAC and MIPS bands, the contaminant list consists of objects in the S-COSMOS IRAC, MIPS 24 and MIPS 70 catalogues that do not match to a source in our optically selected sample with a radius of approximately half the PSF FWHM (1, 3 and 9 arcsec, respectively). We employ a similar technique in the far-IR, matching against the PACS blind catalogues and HerMES StarFinder catalogues with a 3.9, 6.0, 9.0, 12.6 and 18.2 arcsec radius in increasing wavelength order. In bands where PSF convolution is disabled, the minimum aperture radius was set to the PSF FWHM.

Fig. 2 suggests that there will be many objects that lie well below the detection threshold in bands with comparatively low resolution or sensitivity (i.e. the FUV, NUV and mid- to far-IR bands). Attempting to obtain flux for systems significantly below the data sensitivity limits can be problematic. In particular, the LAMBDAR in-built flux-sharing will inevitably downweight bright systems and upweight the faint systems if flooded with targets given the poorer spatial resolution. Although LAMBDAR has been designed to manage this at some level, eventually any algorithm will break down if swamped with thousands of targets where only a few are detectable. Hence, some prudent pruning of the optically selected input and contamination catalogues is necessary for lower resolution and/or

shallower data. Here, we impose a set of cascading flux cuts and prior flux weights to prevent flux being scattered into these objects. UV fluxes have prior weighting (using LAMBDAR's built-in functionality) derived from the LAMBDAR *u*-band photometry, with any object fainter than $u > 24.0$ mag removed from the UV input catalogue. Fluxes in IRAC 1 and 2 were similarly weighted by the *K*-band flux with no cut applied to the target sources, but a $K < 23.5$ mag cut applied to the contaminant list. Fluxes in IRAC 3 and 4 were weighted by IRAC 2, with any source fainter than $i2 < 21.5$ mag and contaminant fainter than $i3 < 22.0$ mag removed. A similar cut of $i4 < 20.5$ was used in MIPS 24. Any source with MIPS 24 flux greater than zero was run in the PACS bands, and sources with $m24 < 19.0$, 18.0, 17.8 and 17.5 were run in SPIRE 250, 350, 500 and MIPS 70, respectively. Contaminants in these bands were weighted by their fluxes as measured in their corresponding catalogues. The IRAC flux cuts are illustrated in Fig. 10.

To construct the photometric catalogue, we run LAMBDAR with the settings shown in Tables 1 and 2. While measuring flux, we apply multiplicative aperture corrections of 1.15 for MIPS 70 (Frayer et al. 2009), 1.50 for PACS 100 and 1.477 for PACS 160, and an additional multiplicative high-pass correction of 1.12 and 1.11 for PACS 100 and 160, respectively.[10]

For PSF convolution, LAMBDAR accepts either an FWHM assuming a Gaussian shape or an empirical PSF provided in a FITS file. We use the Hora et al. (2012) PSF convolution kernels in IRAC 1 and 2, the Gordon et al. (2008) kernels in the remaining IRAC and MIPS bands (100 K for MIPS) and the observed PSF kernels from PEP. *GALEX* convolution kernels were provided by the *GALEX*-GAMA team. For other bands, we use a Gaussian PSF with FWHM given in Table 1.

For MIPS 24 and longer wavelengths, we obtain point source photometry only. This reduces the problem of optically defined large apertures (e.g. of an elliptical galaxy) being no longer appropriate because of the significantly decreased sensitivity in MIPS 24 (see Fig. 2) and declining SEDs. The flux missed will be minimal even in extended sources for the same reasons. Finally, we reconstruct errors in all bands to be the sum of the deblend error, sky rms and sky flux error in quadrature. This omits a shot noise term that was unrealistically large in the *GALEX* and UltraVISTA bands (due to the GAIN assumed by LAMBDAR) and dominated the error budget for the overwhelming majority of objects.

3.5 Star–galaxy separation

In order to robustly identify stars in our photometric catalogue, we perform a multiple stage star-galaxy separation process. First, we apply the star–galaxy flags derived by the COSMOS2015 team. Full details of this process are described in Laigle et al. (2016). Briefly, sources are fit using LE PHARE for both galactic and stellar templates, and best fits derived for both. A source is classed as a star if (i) its best fit $\chi^2_{gal} - \chi^2_{star} > 0$, (ii) it is detected in the NIR or IRAC bands, and (iii) it lies close to the stellar sequence in *BzK* colour space. In addition, the COSMOS2015 catalogue contains a flag to indicate the source is X-ray-detected (and potentially an active galactic nucleus) that we also propagate to our final catalogue.

Following this, we then perform our own stellar identification using the size–magnitude distribution given in Fig. 8. We identify stars are sources with semimajor axis <4 arcsec, semimajor axis $- i < 22$

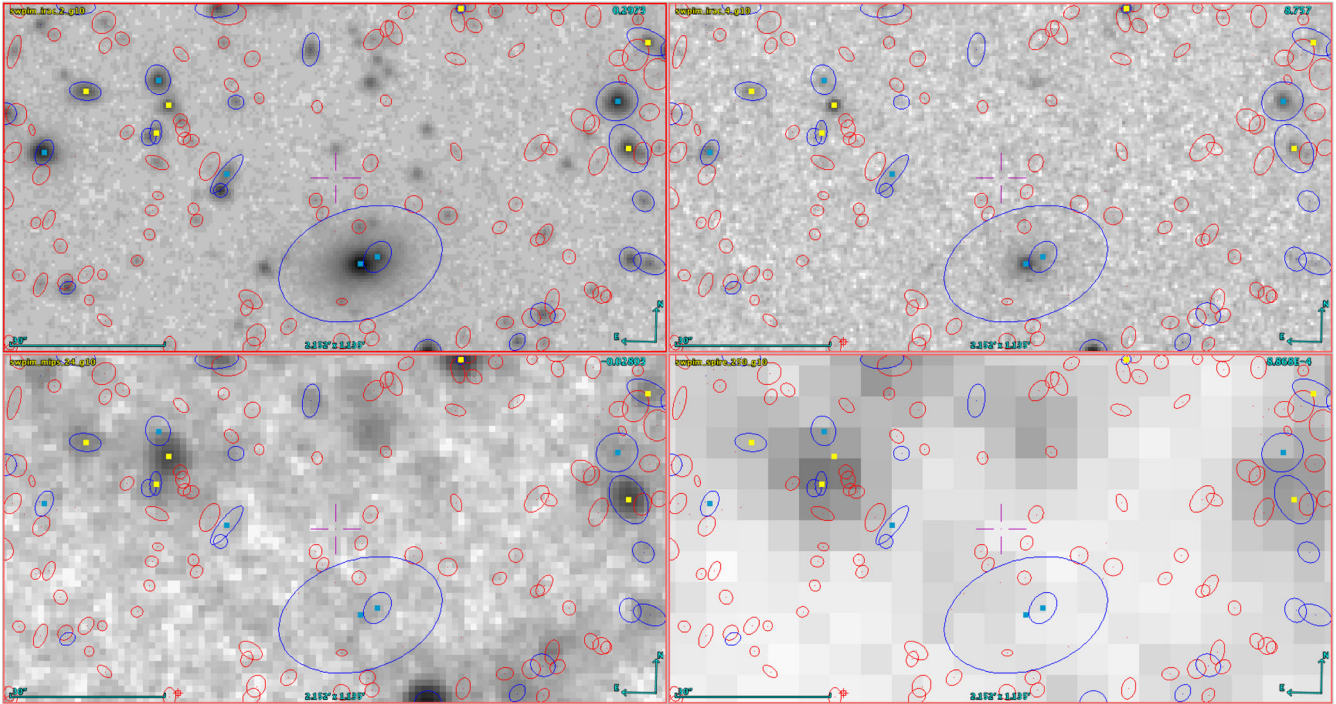[10] http://www.mpe.mpg.de/resources/PEP/DR1_tarballs/readme_PEP_global.pdf

Figure 10. Illustration of the cascading flux cats in the mid- and far-infrared. Images – top left: IRAC 2, top right: IRAC 4, bottom left: MIPS 24, bottom right: SPIRE 250. Sources with yellow dots have both MIPS 24 and SPIRE 250 point source photometry and IRAC 4 photometry measured, blue dots have IRAC 4 and MIPS 24 measurements, blue ellipses have IRAC 4 photometry only and red ellipses have none of these. Each cutout spans an area of 2.15 arcmin × 1.14 arcmin.

Table 2. Instrument-dependant LAMBDAR settings.

Instrument	*GALEX*	Optical, NIR	IRAC	MIPS 24	MIPS 70	PACS	SPIRE
PSFConvolve	Yes	No	Yes	Yes	Yes	Yes	Yes
PixelFluxWgt	Yes	Yes	Yes	Yes	No	Yes	No
PSFWgt	NUV only	No	Yes	Yes	Yes	Yes	Yes
Point sources	No	No	No	Yes	Yes	Yes	Yes
nIterations	5	2	5	5	5	5	5
PSFConfidence	0.95	1	0.95	0.95	0.95	1	1
Prior	$u < 24.0$	–	Section 3.4	$i4 < 20.5$	$m24 < 17.8$	m24 detection	Section 3.4

and $i < 21$ (where i denotes the final LAMBDAR magnitude), displayed in Fig. 8 as the polygon in the bottom left hand corner bounded by the orange and blue lines. The stellar classification from our size–magnitude distribution only supersedes sources that are classified as galaxies by COSMOS2015. For sources that do not have a star–galaxy flag in the COSMOS2015 catalogue (predominantly new sources added in our selection), we apply our size–magnitude flags.

As a final stage, we visually inspect sources in two subsamples and class objects as either a star or galaxy. For all visual inspections, we use cutouts from the HST-F814W data which allows the most robust star–galaxy separation. First, we inspect all ~15 000 sources that are classed as either a star or an X-ray source following the COSMOS2015 and size–magnitude assignments given above. This process identifies any galaxies that have been falsely assigned as stars using our previous selection. Secondly, we visually inspect all sources that have not been identified as stars and are either at $z < 0.06$ (a key epoch in future studies involving this data set) or with i mag < 22 and with no secure spectroscopic redshift (such sources potentially have erroneously bright magnitudes). In total, this sample contains ~5000 sources, of which 385 are identified as stars. These visual classifications then supersede the previous

classifications, resulting in a 'master' star–galaxy separation flag using information from COSMOS2015, our size–magnitude classification and visual inspection, where ~7 per cent of sources in our catalogue are classed as stars, ~92 per cent are classed as galaxies and ~1 per cent as X-ray sources. In total, there are 5539 sources that are visually identified as galaxies, 744 resolved X-ray sources and 831 X-ray point sources.

All individual star–galaxy flags and our resultant 'master' star–galaxy flags are given in our publicly available photometric catalogue.

4 CONSISTENCY CHECKS

4.1 Astrometry

Fig. 11 shows the positional offset between our final aperture catalogue and the pre-existing archival data. The catalogues used for this comparison are COSMOS2015, the 2008 update to the Capak et al. (2007a) catalogue (providing photometric measurements for *GALEX*, CFHT and Subaru), the UltraVISTA DR2 basic blind catalogues, the S-COSMOS IRAC, MIPS 24 and MIPS 70
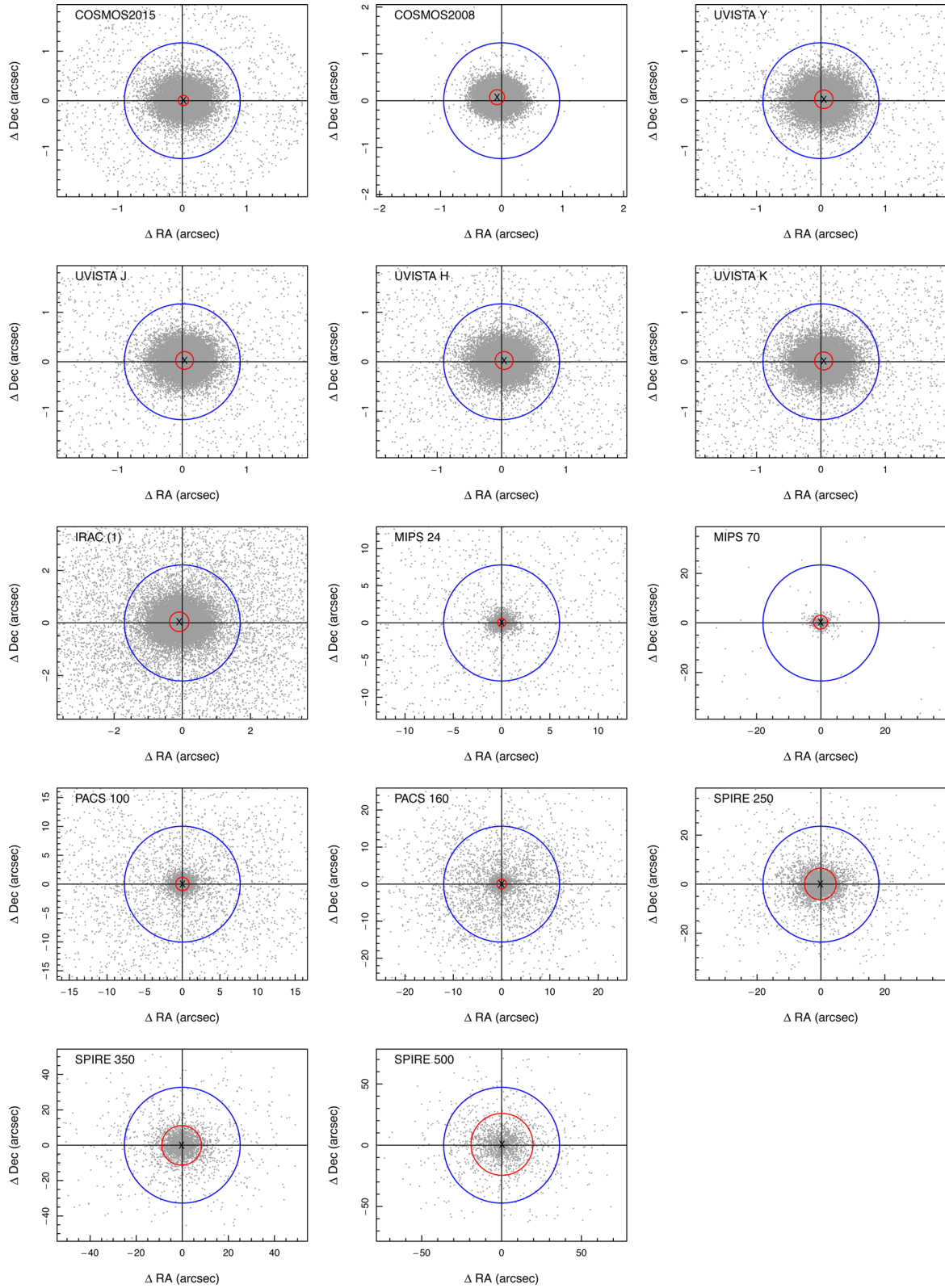
Figure 11. Positional offsets between the aperture catalogue and various archive catalogues. The blue circle shows the PSF FWHM, the black cross the median positional offset and the red circle contains 80 per cent of the population after taking into account random mismatches. When multiple bands are included in the comparison catalogue, the band used is indicated in brackets.
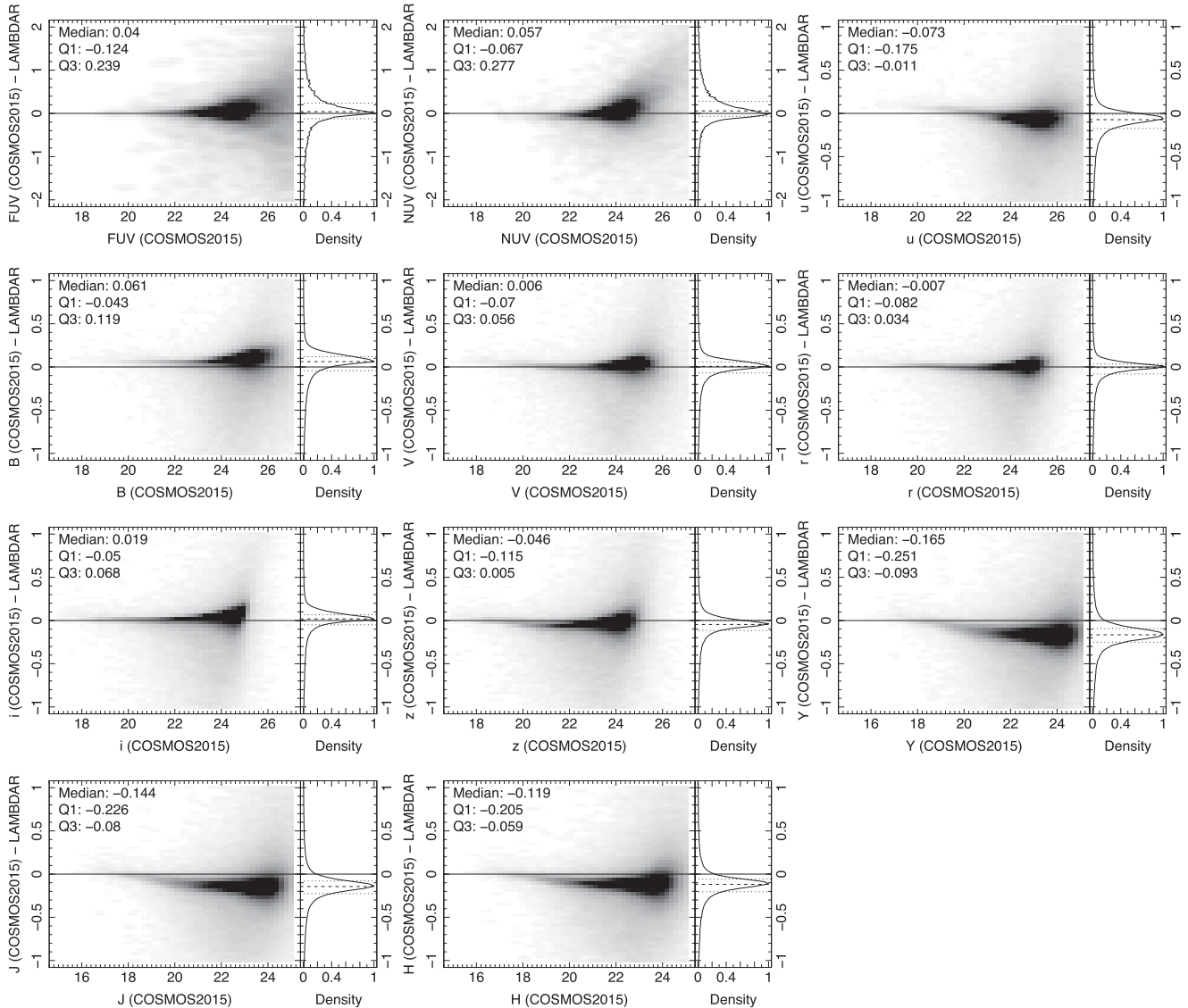
Figure 12. Magnitude offsets between the photometry derived in this work and COSMOS2015; this is a 2D kernel density estimation with square root scaling. The histograms on the right show the 1D distribution and give the median and interquartile range that are also inset in the main panels.

catalogues, the PEP DR1 blind catalogues and the HerMES DR2 StarFinder catalogues. For this analysis, positional matches were performed with a radius of three times the PSF FWHM except for COSMOS2015 and COSMOS2008, where exact ID matches were used.

The centroids in the figure, depicted by the black cross and computed after removing random mismatches from the sample, demonstrate that our astrometry is robust to within 0.12 times the PSF FWHM. For the optical data, this translates to an astrometric accuracy of 0.106 arcsec. In all other cases, the centroid is within 0.1 arcsec, apart from the low-resolution far-IR bands (MIPS 70 and SPIRE), where it remains below 0.75 arcsec. 66 per cent of the data, as delineated by the red circle, is contained with 0.2 times the PSF FWHM at all wavelengths except for the SPIRE bands. Sources mismatching outside the PSF (as denoted by the blue circle) are generally small extended objects (1–2 arcsec). From this, we conclude that our astrometric accuracy is as expected given the PSF FWHM, apart from potentially SPIRE 500 where the resolution and sensitivity are the lowest.

4.2 Comparisons with existing photometry

Fig. 12 compares magnitudes derived from LAMBDAR and the COS-MOS2015 catalogue (Laigle et al. 2016) (AUTO magnitudes). For these comparisons, saturated and masked objects are removed. An exact match for the 2008 COSMOS ID was performed. A value above zero in this figure indicates that LAMBDAR recovers more flux than the comparison catalogue and vice versa.

Our photometric measurements are broadly consistent with the COSMOS2015 photometry, with two exceptions. In the NIR, our catalogue is consistent with the UltraVISTA DR2 blind detections. The offset from COSMOS2015 may be due to differences in aperture definition or choice of selection image. In IRAC 4, our catalogue is consistent with S-COSMOS. The photometry for the Subaru narrow-bands, while not shown in Fig. 12, is also consistent with the COSMOS2015 catalogue. While not apparent in Fig. 12, a population of objects with $24.5 < i < 25$ may have apertures that are an erroneous combination of objects near or below $i = 25$ mag. This arises from the hard flux cut being made in the LAMBDAR input
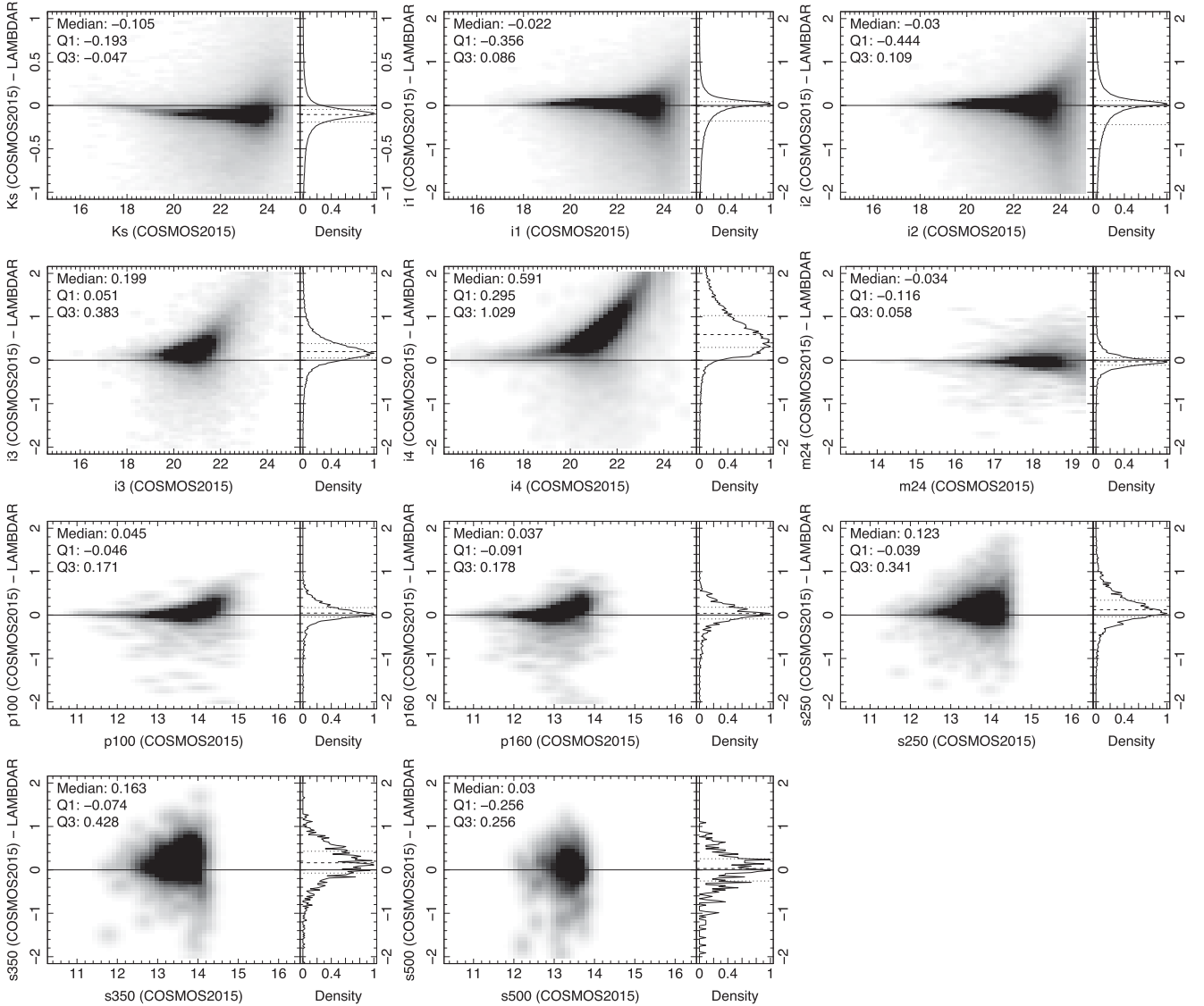
Figure 12 – *continued*

catalogue. For similar reasons, our catalogue contains 18 323 objects not in COSMOS2015. Therefore, fluxes for objects with $i > 24.5$ mag or not in COSMOS2015 should be treated with caution.

4.3 Colour distributions

The plots shown in Fig. 12 are useful for diagnosing zero-point and linearity problems, but do not give an objective assessment as to which data set is more robust. In order to shed light on this, we examine distributions of adjacent colours across all broad-bands. A sample of galaxies will have some intrinsic colour distribution, which is then convolved with error distributions introduced by the instrumentation, observing conditions, photometric data reduction methods and photometric measurement error. A narrower colour distribution and a lower outlier fraction – indicating a narrower photometric error distribution if the same images and galaxies are used – are, hence, more desirable.

To this extent, we compare our colours to those derived from the archival photometry detailed in Section 4.1, COSMOS2015,

Muzzin et al. (2013) (*r* band-selected) and CFHT-Legacy Survey (CFHT-LS) in Fig. 13. In this comparison, we use the COSMOS2015 AUTO magnitudes. Muzzin et al. (2013) derived PSF matched 2.1 arcsec photometry based on the publicly available *GALEX*, CFHT, Subaru, UltraVISTA, S-COSMOS IRAC and MIPS 24 imagery detailed in Section 2. CFHT-LS independently surveyed a 1 $\deg^2$ portion of the COSMOS region in the MegaPrime *ugrizy* filters, achieving 80 per cent completeness at $i = 25.5$ mag. The corresponding CFHT-LS catalogue contains AUTO magnitudes that are converted to the Subaru filterset via the equations in Capak et al. (2007a).

For these comparisons, catalogues were matched with the radii given in Section 4.2 and saturated and masked objects are removed. This is a matched sample, meaning that the colour distributions reflect only sources that are in our catalogues, the archival catalogue and the COSMOS2015 catalogue. The red, green, and blue curves show the subset of the matched sample that have Muzzin et al. (2013) and CFHT-LS photometric measurements. As the imaging data used are common to all sets apart from CFHT-LS, it is only the photometric measurement that is being tested.
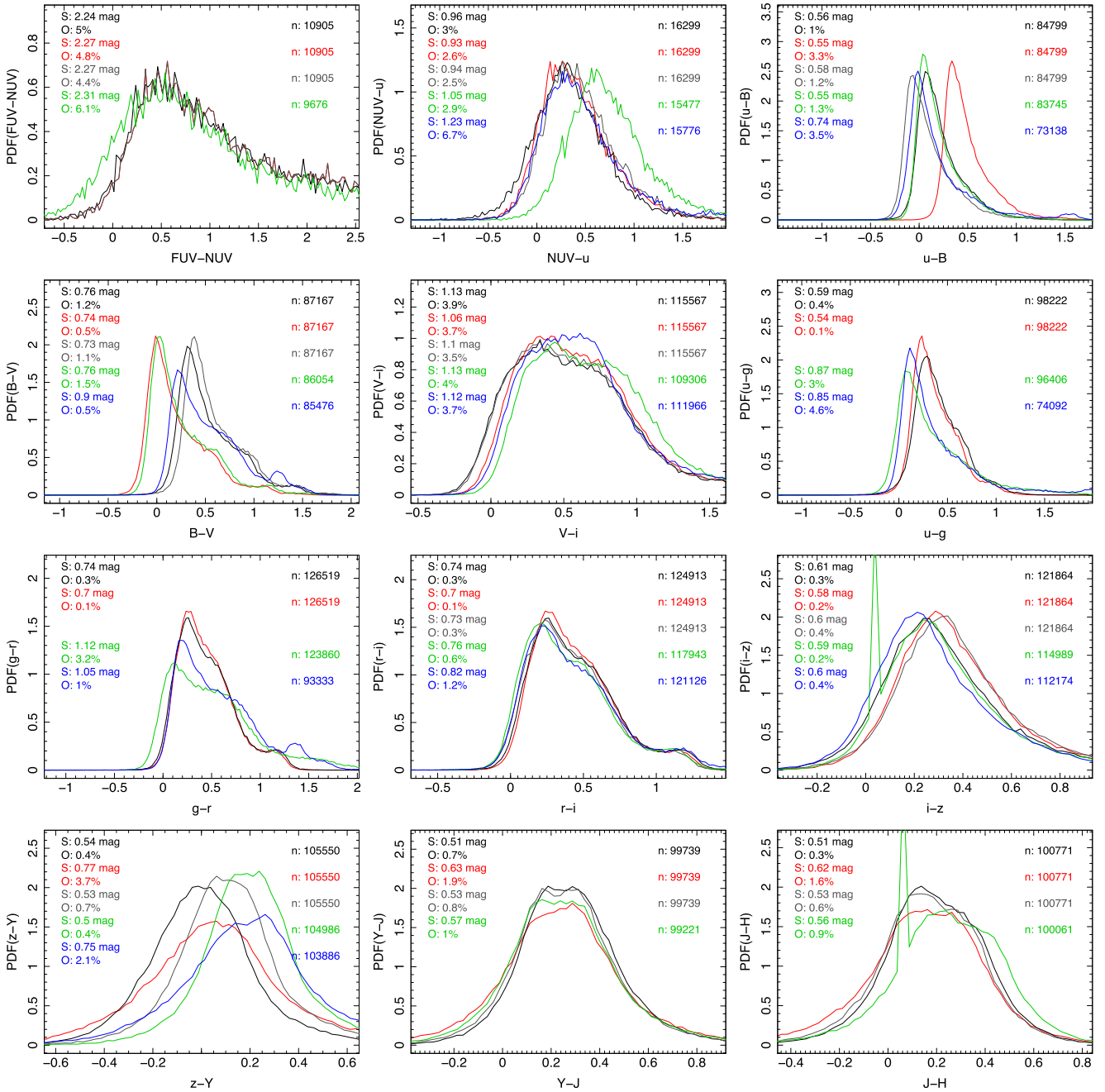
Figure 13. PDFs of colour distributions for adjacent filters (as indicated) for the LAMBDAR (black), archival (red), Laigle et al. (2016) (grey), Muzzin et al. (2013) (green) and CFHT-LS (blue) photometry. The 80th percentile spread and outlier rate (objects that lie outside 0.5 mag of the 80th percentile range) are denoted by S and O, respectively. A flux cut of 0.5 mag fainter than the peak of the number counts in each band of our catalogue was applied to all data sets.

To indicate the width of the colour distribution, we somewhat arbitrarily use the 80th percentile spread. To determine the rate of gross photometric errors, we define outliers to be objects that lie 0.5 mag outside the 80th percentile of each colour distribution. It is plausible that objects have intrinsic colours that fall within this region, especially when the underlying colour distribution and/or redshift range are broad. This is particularly noticeable at optical wavelengths, where the broad distribution of rest-frame FUV, NUV and *u*-band emission arising from the wide variance between star-forming and passive systems has been redshifted into *B*, *V*, *g* and *r* and superimposed on lower redshift objects. However, in the near-

IR where the intrinsic spread is the lowest, the outlier rate almost purely reflects gross photometric errors.

We find that our catalogue is comparable to the COSMOS2015 AUTO colours in nearly all bands. Our catalogue is also comparable to the other, existing catalogues, while avoiding the spikes in $i - z$ and $J - H$ and the colour offsets in $K - i1$ and $i4 - m24$ seen in the Muzzin et al. (2013) catalogue. The inconsistency between the data sets for the Subaru *B* filter is due to the zero-point calibration being uncertain at the time of the 2008 COSMOS photometric catalogue.

The boundaries between the different data reduction techniques (NUV$-u$, $z - Y$, $K_s - i1$, $i4 - m24$, $m24 - m70$, $m70 - p100$,
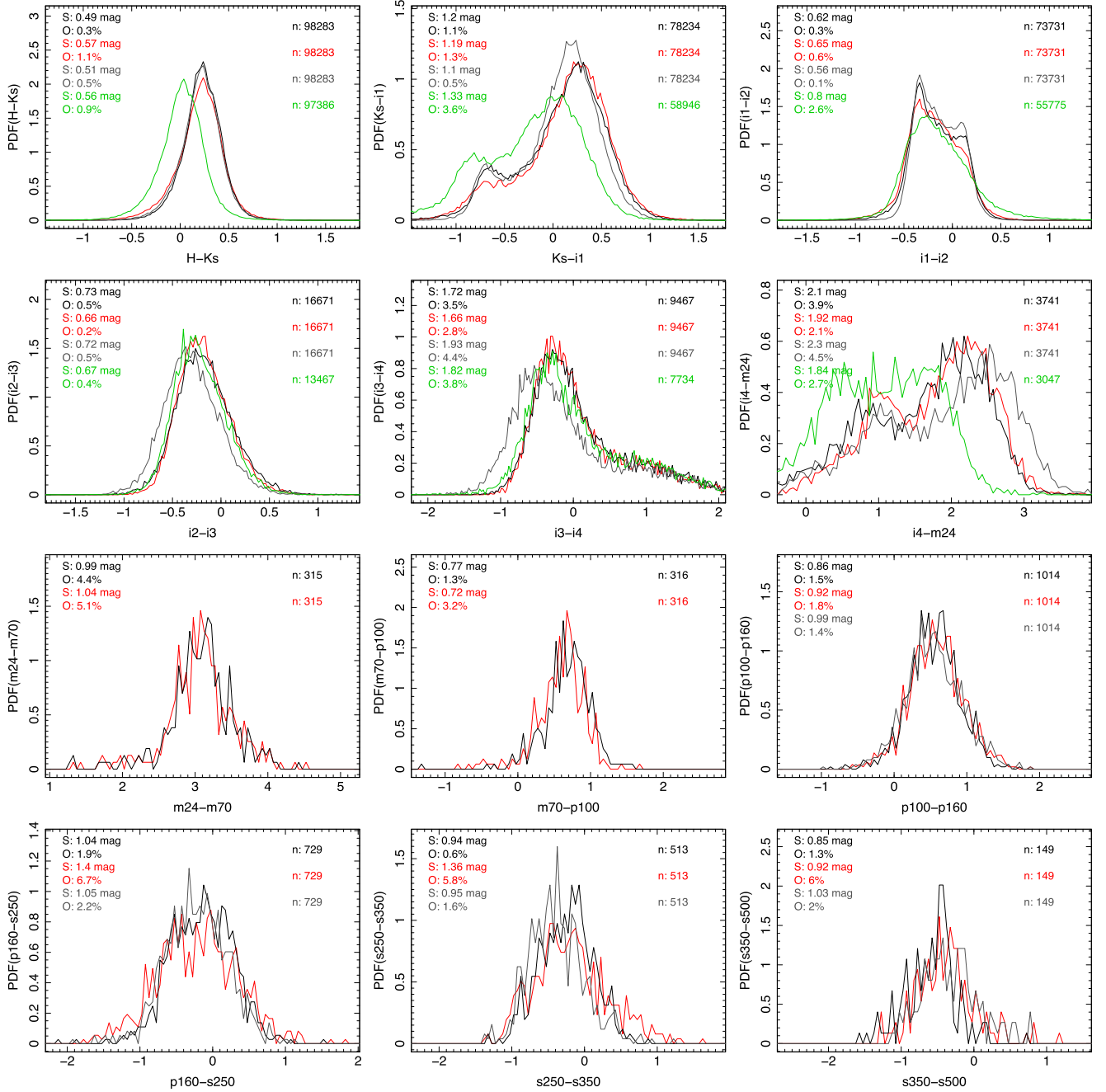
Figure 13 – *continued*

$p160 - s250$) are also of interest because they highlight the non-homogenous nature of the existing photometry that manifests in colour offsets between the different data sets. These boundaries also exhibit increased outlier rates due to the potential for table mismatches and zero-point errors.

Our catalogue generally has comparable errors to the archival photometry in the optical, MIPS and PACS passbands and *GALEX*. The use of LAMBDAR to derive consistent errors across the wavelength range should represent a significant improvement over table matching archival catalogues at least three further aspects. First, no aperture corrections are provided for the errors in the archival catalogues and a simple scaling is likely to underestimate the expanded error. Secondly, the use of SEXTRACTOR to derive errors in

the archival UltraVISTA and IRAC catalogues may lead to errors being systematically underestimated (see Hill et al. 2011). Finally, LAMBDAR incorporates a (conservative) estimate of the uncertainty in deblend solutions, leading to more realistic errors for objects in crowded regions.

4.4 SED fitting

To highlight the benefits in producing a consistent total flux catalogue for full SED analysis and as a prelude to future investigations, we fit SEDs to 5619 sources (IDs 6000000 to 6006500) using MAGPHYS (Multiwavelength Analysis of Galaxy Physical Properties; da Cunha, Charlot & Elbaz 2008) for both our catalogue,

Figure 14. Top: *Kiu* cutouts for IDs 6001044 (top), 6001033 (centre) and 6001075 (bottom). Other panels: MAGPHYS fits for using the LAMBDAR photometric catalogue produced in this work (centre), the same but using COSMOS2015 photometry (right) for IDs 6001044 (top) and 6001033 (centre) and archival photometry for 6001075 (bottom). Black line: attenuated SED, grey line: unattenuated SED, blue points: attenuated SED convolved with the respective filters, green points: archival photometry, grey points: COSMOS2015 photometry, red points: our photometric catalogue. Z_GEN, from Davies et al. (2015a), denotes the genesis of the redshift measurement; the three examples presented above have secure spectroscopic redshifts from zCOSMOS data.

COSMOS2015 (AUTO magnitudes) and the archival photometry detailed in Section 4.1. The sample size was selected to give a quick look into the data set while keeping CPU and manual inspection time requirements at a manageable level. Of these sources, ∼98 per cent have high-resolution spectroscopic redshifts. We look to use MAGPHYS as a means of providing a representative interpolation function for the various photometric measurements. Uniform broad-band coverage across a wide wavelength range is more important for SED fitting than the density of sampling within that range. In our fits, we use the wideband filters excluding *B* and *V*, except for COSMOS2015 that uses these filters instead of *g* and *r*.

Fig. 14 shows example fits using our catalogue (left) and COSMOS2015 or the archival photometry (right). The top panel shows a situation where the deblending of LAMBDAR is likely to be superior. The centre panel shows 6001033 that is deblended into two objects in our catalogue and is one object in COSMOS2015. Similarly, a clear break occurs between *z* and *Y* in the archival photometry for 6001033 due to different deblend solutions and methods. The erroneously high *Y*-band measurement for 6001075 in the archival catalogue is due to a large, incorrect aperture that loops around a

nearby bright source. In this case, the COSMOS2015 fit is similar to the LAMBDAR fit, with a noticeable difference in the far-IR.

The χ^2 distribution for all three data sets is shown in Fig. 15. Broadly speaking, our catalogue achieves a χ^2 distribution that is more balanced and centred on the expected $\chi^2 = 1$ compared to both COSMOS2015 and the archive data sets. 3174 of the 5579 common objects have a χ^2 closer to one in our catalogue compared to COSMOS2015. Note that the COSMOS2015 catalogue is optimized for accurate colours, while we aim to measure total fluxes. Compared to the archive, 3704 of the 5619 common objects have a χ^2 closer to one with our catalogue. The improvement in χ^2 is partly due to the incorporation of deblend errors into our catalogue, particularly for the IRAC bands. However, with a visual inspection, it becomes clear that at least some of the improvement over the archive is due to the use of consistent photometry and wavelength errors across the wavelength range.

These comparisons are inevitably complicated by the ability of MAGPHYS to correctly model galaxies at intermediate redshifts. This will be discussed in more detail in Driver et al., in preparation, where we fit the entire GAMA and G10/COSMOS samples using both
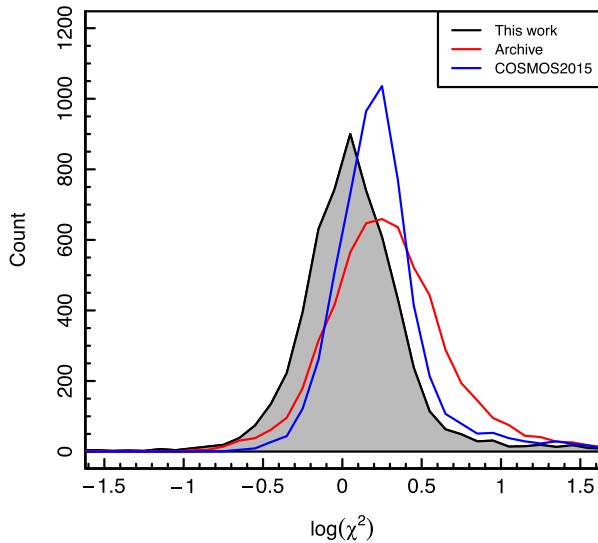
Figure 15. The $\log(\chi^2)$ distribution of MAGPHYS fits using both our catalogue, the archival photometry and COSMOS2015 for approximately 5600 sources. Bin size is 0.1 in $\log(\chi^2)$.

this and the Wright et al. (2016) catalogues. Using these data sets, we will examine the cosmic SED (Andrews et al., in preparation), star formation rates (Davies et al., in preparation), stellar masses (Wright et al., in preparation) and validate and improve the SED fitting process out to $z = 1$.

5 RELEASE CONTENT

We release three sets of catalogues. The main catalogue contains abridged redshift information from Davies et al. (2015a) and fluxes and errors for each band in Janskys. This catalogue contains fluxes corrected for Galactic extinction for *FUV* to K_s inclusive using the $E(B - V)$ values from the Schlegel, Finkbeiner & Davis (1998) dust maps multiplied by the $k(\lambda)$ values given in Table 3. Objects which have a greater than 0.8 arcsec positional offset between this catalogue and the 2008 COSMOS photometric catalogue have been assigned a FLAGS value of 1. To denote masked regions, we propagate the relevant COSMOS2015 flag column. Non-matches to COSMOS2015 are assigned a mask value equal to their nearest neighbour. For objects that do not have flux measurements due to cascading flux cuts, we assign a flux of -9998 and an error equal to the 1σ point source limit as calculated from the median sky rms for 1000 random apertures (see Fig. 2). The fraction of objects assigned upper limits range from 82 per cent in the UV, 81 per cent for IRAC 3 and 4, 94 per cent for MIPS 24 and PACS, 96 per cent for SPIRE 250, 98 per cent for SPIRE 350 and 99 per cent for SPIRE 500 and MIPS 70. These are shown by the bottom panel of Fig. 16.

Fig. 16 attempts to summarize our panchromatic catalogue as compared to COSMOS2015, and what one might construct from existing archival photometry. The upper three panels show, for each catalogue, the colour distribution for the same set of galaxies. The vertical spread therefore indicates a colour range ($x - K$; where x represents each filter in turn), each colour band denotes a filter (x) and the horizontal spread the redshift range ($0.4 < z < 0.8$). The density of data points reflects the number of objects. To create the sample, the three catalogues were matched and only those galaxies with $f > \delta f$ for both K and x in all three catalogues selected. The fourth panel shows the widths of the colour distribution as measured from the 84th–16th percentile range (i.e. 1σ) that are

Table 3. Galactic extinction corrections.

Band	$k(\lambda)$
FUV	8.376[a]
NUV	8.741[a]
u	4.690[b]
B	4.039[b]
V	3.147[b]
g	3.738[b]
r	2.586[b]
i	1.923[b]
z	1.436[b]
IA427	4.260[c]
IA464	3.843[c]
IA484	3.621[c]
IA505	3.425[c]
IA527	3.264[c]
IA574	2.937[c]
IA624	2.694[c]
IA679	2.430[c]
IA709	2.289[c]
IA738	2.150[c]
IA767	1.996[c]
IA827	1.747[c]
NB711	2.268[c]
NB816	1.745[b]
Y	1.211[d]
J	0.871[d]
H	0.563[d]
K_s	0.364[d]

Notes. [a]Liske et al. (2015).
[b]Capak et al. (2007a).
[c]Laigle et al. (2016).
[d]McCracken et al. (2012).

essentially comparable for all data sets. Finally, the bottom plot shows the fraction of objects with a 1σ detection (dashed line) or a limit (solid line). From the u to K bands, all catalogues contain a measurement for all objects. In the FUV, NUV and IRAC bands, a recorded strong or credible measurement occurs more frequently in the COSMOS2015 catalogue, and in the far-IR, our catalogue contains more credible measurements than either COSMOS2015 or archival data. However, the critical advancement is that our catalogue now contains a measurement or flux limit for every object, essentially increasing the fraction of systems with far-IR constraints from a few per cent to all galaxies in all bands.

Additionally, we release the catalogues output by LAMBDAR for each of the 38 bands that provide more detailed photometric measurements and errors, as separate files. These catalogues also contain warning flags, such as for objects affected by the saturated NaN region replacement detailed in Section 3.4. The fluxes contained in these catalogues are not extinction-corrected.

In addition to the new photometry catalogues presented in the work, we also highlight the release of an updated version of the spectroscopic catalogue outlined in Davies et al. (2015a). This catalogue now incorporates DR3 of the zCOSMOS (Lilly et al. 2007) spectra, released in 2015 January (ESO Large Programme LP175.A-0839) and the recent photometric redshift analysis of the COSMOS2015 team (Laigle et al. 2016). Columns 135–139 of the Davies et al. catalogue are updated with the zCOSMOS DR3 measurements and additional columns, 176–179, are added for the COSMOS2015 best-fitting redshift ('ZP_COSMOS2015'), the 1σ upper and lower error range ('ZL68_COSMOS2015' and 'ZH68_COSMOS2015'), and the best-fitting χ^2 value ('CHI2_COSMOS2015'). We also
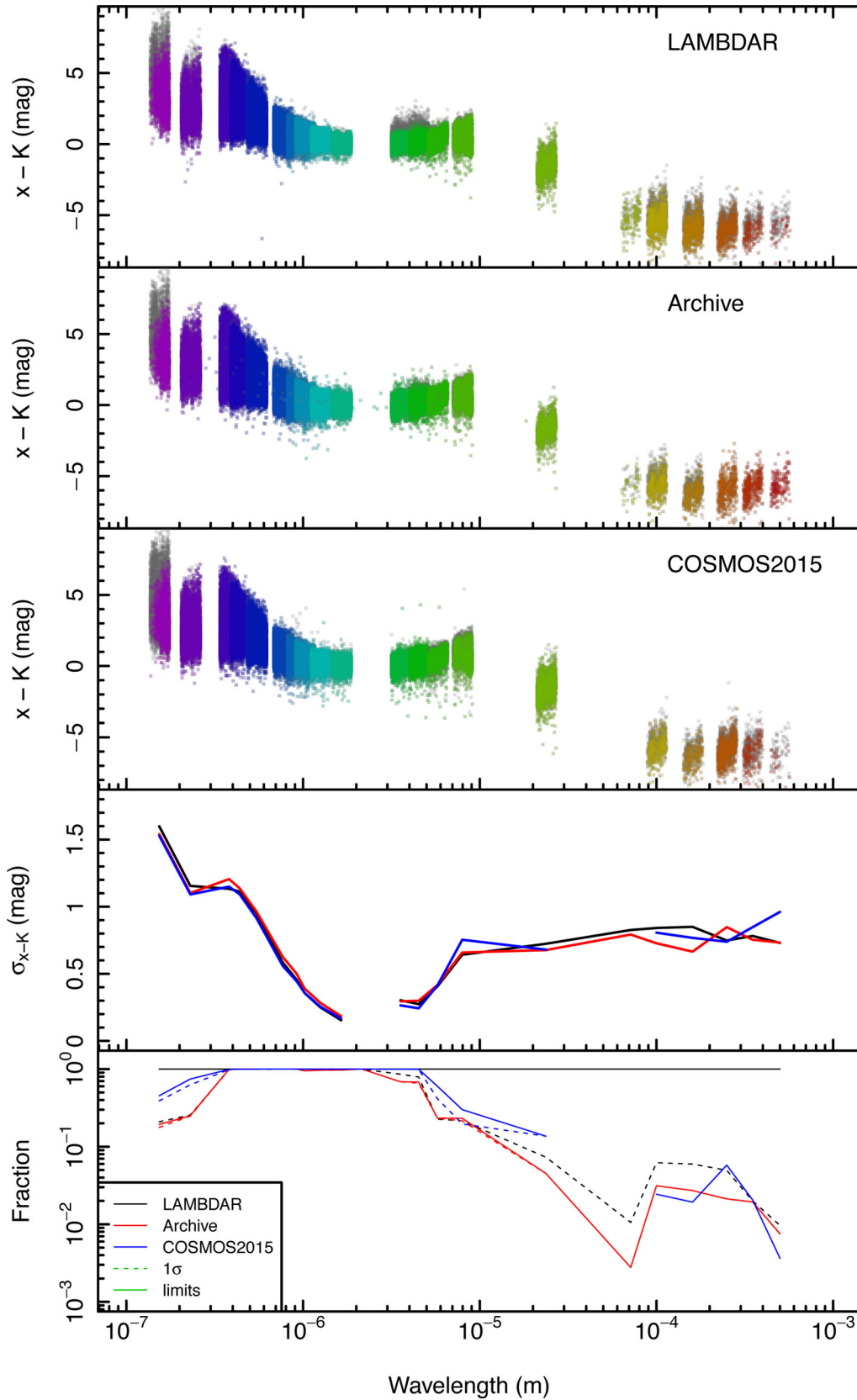
Figure 16. Top three panels: colour spreads with respect to *K* for the indicated data sets. 5σ detections are coloured, while 1σ detections are in grey. Fourth panel: the spread of the *x − K* colour distributions, as given by half of the difference between the 84th and 16th percentiles. Bottom panel: fraction of objects with upper limits (solid line) and 1σ (dashed line) detections.

update the 'Z_BEST', 'Z_USE' and 'Z_GEN' parameters accordingly. To do this, we undertake a similar process to that outlined in section 4 of Davies et al. (2015a), where we compare redshift measurements across various observations. However, we now perform matching in comparison to the zCOSMOS DR3 catalogue instead of the zCOSMOS-bright 10k catalogue, and to the more recent COSMOS2015 photometric redshifts over the original Ilbert et al. (2009) photometric redshifts. For example, Z_GEN==5 now refers to a <10 per cent offset between our AUTOZ measurement and the COSMOS2015 photometric redshift.

This updated catalogue yields an increased number of Z_USE==1 sources (good high-resolution redshift), increasing the sample to ∼19*k* galaxies, and slightly reducing the spread and outlier rate of comparisons between Z_BEST and zCOSMOS/PRIMUS/photometric redshifts, as displayed in fig. 9 of Davies et al. (2015a). We refer the reader to Davies et al. (2015a) for further details of how the spectroscopic catalogue was constructed and note that the updated catalogue can be found here: http://cutout.icrar.org/G10/G10CosmosCatv03.tar.gz.

6 CONCLUSION

We have produced a 38 band photometric catalogue in COSMOS spanning from FUV to far-IR wavelengths in a manner consistent with the equivalent Wright et al. (2016) GAMA catalogue. We gathered multiwavelength imagery from the *GALEX* Deep Imaging Survey, COSMOS, UltraVISTA, S-COSMOS, SPLASH, PEP and HerMES surveys. From these data, we obtained consistent total flux measurements for a sample of 185 907 sources using LAMBDAR. This required the construction of an aperture catalogue by manually checking and adjusting raw SEXTRACTOR output, a process that is prohibitively labour-intensive for the next generation of galaxy surveys. We demonstrate that the resulting photometric catalogue has accurate astrometry that is consistent with existing photometric data sets and achieves adjacent colour distributions – a proxy for photometric measurement error – comparable to existing data sets. The released catalogue is complete for objects with *i* < 24.5 mag and partially complete to *i* < 25 mag due to a rigid flux cut made prior to the LAMBDAR measurements. As our catalogue is designed for panchromatic analysis, including SED fitting, we tested it for a sample of 5619 galaxies using MAGPHYS. We found improved convergence and goodness of fit with our catalogue compared to table matching archival photometry. The catalogues and a cutout generator for the multiwavelength imagery used are available at http://cutout.icrar.org/G10/dataRelease.php.

This sample will be used in future observations as an input catalogue for a spectroscopic survey to complete the G10 region. This catalogue will form the basis for a GAMA-equivalent multiwavelength data base at intermediate redshifts. This data base will enable the derivation of physical properties and structural parameters for the COSMOS region using the same techniques as GAMA and enable comparative studies of the cosmic SED (Andrews et al., in preparation), galaxy structure and morphology, star formation rates (Davies et al., in preparation), stellar masses (Wright et al., in preparation) and panchromatic measurements of the extragalactic background light (Driver et al. 2016c). In combination with further spectroscopic observations of the G10 region, we will create catalogues of groups (akin to Robotham et al. 2011) and large-scale structure.

In addition to enabling comparisons to low-redshift galaxy evolution surveys, these catalogues will pave the way for future galaxy evolution surveys such as WAVES (Driver et al. 2016a) and provide

a basis for optically motivated stacking using 21 cm data from the COSMOS HI Large Extragalactic Survey (Fernández et al. 2013).

REFERENCES

Ahn C. P. et al., 2014, ApJS, 211, 17
Alpaslan M. et al., 2014, MNRAS, 438, 177
Aune S. et al., 2003, in Iye M., Moorwood A. F. M., eds, Proc. SPIE Conf. Ser. Vol. 4841, Instrument Design and Performance for Optical/Infrared Ground-based Telescopes. SPIE, Bellingham, p. 513
Baldry I. K. et al., 2014, MNRAS, 441, 2440
Bertin E., Arnouts S., 1996, A&A, 117, 393
Bertin E. et al., 2002, in Bohlender D. A., Durand D., Handley T. H., eds, ASP Conf. Proc. Vol. 281, Astronomical Data Analysis Software and Systems XI. Astron. Soc. Pac., San Francisco, p. 228
Boulade O. et al., 2003, in Iye M., Moorwood A. F. M., eds, Proc. SPIE Conf. Ser. Vol. 4841, Instrument Design and Performance for Optical/Infrared Ground-based Telescopes. SPIE, Bellingham, p. 72

Brammer G. B. et al., 2012, ApJS, 200, 13
Capak P. et al., 2007a, ApJS, 172, 99
Capak P., Abraham R. G., Ellis R. S., Mobasher B., Scoville N., Sheth K., Koekemoer A., 2007b, ApJS, 172, 284
Coil A. L. et al., 2011, ApJ, 741, 8
Cool R. J. et al., 2013, ApJ, 767, 118
da Cunha E., Charlot S., Elbaz D., 2008, MNRAS 388, 1595
Davies L. J. M. et al., 2015a, MNRAS, 447, 1014
Davies L. J. M. et al., 2015b, MNRAS, 452, 616
Davies L. J. M. et al., 2016a, MNRAS, 461, 458
Davies L. J. M. et al., 2016b, MNRAS, 455, 4013
de Jong J. T. A. et al., 2015, A&A, 582, A62
Driver S. P. et al., 2011, MNRAS, 413, 971
Driver S. P. et al., 2012, MNRAS, 427, 3244
Driver S. P., Davies L. J., Meyer M., Power C., Robotham A. S. G., Baldry I. K., Liske J., Norberg P., 2016a, Proc. Astrophysics and Space Science, Vol. 42, The Universe of Digital Sky Surveys. Springer Int. Publ., Switzerland, p. 205
Driver S. P. et al., 2016b, MNRAS, 455, 3911
Driver S. P. et al., 2016c, ApJ, 827, 108
Eales S. et al., 2010, PASP, 122, 499
Edge A., Sutherland W., Kuijken K., Driver S. P., McMahon R., Eales S., Emerson J. P., 2013, The Messenger, 154, 32
Fernández X et al., 2013, ApJ, 770, L29
Frayer D. T. et al., 2009, AJ, 138, 1261
Garilli B. et al., 2008, A&A, 486, 683
Gordon K. D., Engelbracht C. W., Rieke G. H., Misselt K. A., Smith J.-D. T., Kennicutt R. C., 2008, ApJ, 682, 336
Griffin M. J. et al., 2010, A&A, 518, L3
Hill D. T. et al., 2011, MNRAS, 412, 765
Hora J. L. et al., 2012, Proc. SPIE, 8442, 39
Hsieh B.-C., Wang W.-H., Hsieh C.-C., Lin L., Yan H., Lim J., Ho P. T. P., 2012, ApJS, 203, 23
Ilbert O. et al., 2009, ApJ, 690, 1236
Ilbert O. et al., 2015, A&A, 579, A2
Kelvin L. S. et al., 2012, MNRAS, 421, 1007
Komiyama Y. et al., 2003, in Iye M., Moorwood A. F. M., eds, Proc. SPIE Conf. Ser. Vol. 4841, Instrument Design and Performance for Optical/Infrared Ground-based Telescopes. SPIE, Bellingham, p. 152
Laidler V. G. et al., 2007, PASP, 119, 1325
Laigle C. et al., 2016, ApJS, 224, 24
Lawrence A. et al., 2007, MNRAS, 379, 1599
Le Févre O. et al., 2015, A&A, 576, A79
Le Floc'h E. et al., 2009, ApJ, 703, 222
Levenson L. et al., 2010, MNRAS, 409, 83
Lilly S. J. et al., 2007, ApJS, 172, 70
Lilly S. J. et al., 2009, ApJS, 184, 218
Liske J. et al., 2015, MNRAS, 452, 2087
Loveday J. et al., 2015, MNRAS, 451, 1540
Lutz D. et al., 2011, A&A, 532, A90
McCracken H. J. et al., 2012, A&A, 544, A156
Martin C. et al., 2005, ApJ, 619, 1
Masters D. et al., 2012, ApJ, 755, 2
Moffett A. et al., 2016, MNRAS, 457 1308
Muzzin A. et al., 2013, ApJS, 206, 8
Oliver S. J. et al., 2012, MNRAS, 424, 1614
Pilbratt G. L. et al., 2010, A&A, 518, L1
Poglitsch A. et al., 2010, A&A, 518, L2
Riguccini L. et al., 2015, MNRAS, 452, 470
Robotham A. S. G. et al., 2011, MNRAS, 416, 2640
Roseboom I. G. et al., 2010, MNRAS, 409, 48
Sanders D. B. et al., 2007, ApJS, 172, 86
Schlegel D. J., Finkbeiner D. P., Davis M., 1998, ApJ, 500, 525
Scoville N. et al., 2007, ApJS, 172, 1
Silverman J. D. et al., 2015, ApJS, 220, 12
Smith A. J. et al., 2012, MNRAS, 419, 377
Taniguchi Y. et al., 2007, ApJS, 192, 9
Taniguchi Y. et al., 2015, PASJ, 67, 104
Taylor E. N. et al., 2011, MNRAS, 418, 1587
Viero M. P. et al., 2013, ApJ, 772, 77
Wang L. et al., 2014, MNRAS, 444, 2870
Wright E. L. et al., 2010, AJ, 140, 1868
Wright A. H. et al., 2016, MNRAS, 460, 765
York D. et al., 2000, AJ, 120, 1579
Zamojski M. A. et al., 2007, ApJ, 172, 468

This paper has been typeset from a T_EX/L^AT_EX file prepared by the author.